Journal of Materials Chemistry A

ROYAL SOCIETY OF CHEMISTRY

REVIEW

View Article Online
View Journal

Cite this: DOI: 10.1039/d0ta08869b

Recent advances in solar-driven evaporation systems

Zhourui Xu, [ae] Zida Li,[a] Yihang Jiang, [a] Gaixia Xu, [a] Mingwei Zhu,[b] Wing-Cheung Law, [c] Ken-Tye Yong, [d] Yanshuai Wang,[e] Chengbin Yang,[a] Biqin Dong [e] and Feng Xing*[e]

Nowadays, energy and the environment have become critical issues for determining the sustainability of the Earth. Freshwater crises, as an increasingly serious global problem, pose a great threat to our economies, the environment and us. Solar-driven evaporation has emerged as a promising and sustainable approach to convert solar energy into clean water. In fact, the production of freshwater is not only governed by heat generation at the interface, but the process also relies on the coordination and cooperation of functional modules in the solar-driven evaporation system. This review begins with system designs of solar evaporators, considering thermal manipulation structures, water transportation pathways, and vapour condensation modules, which focus on improving the overall energy utilization, long-term usability, and freshwater yield. This is followed by a summary and discussions of cutting-edge solar evaporation applications and their underlying mechanisms. Finally, existing challenges and potential solutions for future applications are discussed and provided. This review aims to provide useful guidelines and references to scientists and researchers for the future development of clean water generation systems.

Received 9th September 2020
Accepted 30th October 2020

DOI: 10.1039/d0ta08869b

rsc.li/materials-a

1. Introduction

With the ever-growing population on the Earth within the past century, water scarcity has become one of the major threats to human society.[1] In this age, nearly two-thirds of the world's population live under the shadow of water shortage.[2,3] In recent decades, huge efforts have been devoted to developing efficient and reliable methods to tackle water scarcity issues. However, the existing technologies which have been applied for large-scale water supply were invented at the expense of aggravating energy problems[4–6] or, even worse, overly exploiting the environment,[4,7] and are certainly not long-term solutions. Therefore, sustainable and economical technologies for freshwater production are urgently needed.

Solar-driven vapor generation, which utilizes sunlight as the energy source to accelerate vapor production from the sea, is a promising approach to alleviate the severe situation of water scarcity with minimal environmental impacts.[8] Over the past decade, the strategy of solar vapor generation has undergone a rapid evolution from a volumetric configuration,[9,10] in which the photothermal agents are suspended or dispersed in water to thermalize the bulk water, to an interfacial configuration, in which solar evaporators float at the air–water interface to achieve localized heating, with increasing understanding of thermal utilization. Compared with volumetric heating, interfacial heating actively confines thermal energy at the water surface and reduces the heat loss to the bulk water, resulting in an enhanced water evaporation rate. In addition, the facile preparation,[11] automatic operation,[12] and low capital investment[13,14] features of solar-driven evaporation endow it with great potential for deployment especially in off-grid and remote areas. In view of its advantages, great efforts have been devoted by scientists in the past few years to developing an interfacial-based solar evaporator with the ultimate goal of freshwater production.

Although huge progress has been made in the field of solar evaporation, from a practical point of view, current solar evaporators still suffer from immature energy and water manipulation, resulting in unsatisfactory freshwater productivity. The basic concept behind solar vapor generation involves several sub-processes, including optical and thermal energy

[a]Guangdong Key Laboratory for Biomedical Measurements and Ultrasound Imaging, School of Biomedical Engineering, Shenzhen University Health Science Center, Shenzhen, 518060, China

[b]National Laboratory of Solid State Microstructures, College of Engineering and Applied Sciences, Nanjing University, Nanjing 210093, China

[c]Department of Industrial and Systems Engineering, The Hong Kong Polytechnic University, 11 Yuk Choi Road, Kowloon, Hong Kong, China

[d]School of Electrical & Electronic Engineering, Nanyang Technological University, 639798, Singapore

[e]Guangdong Provincial Key Laboratory of Durability for Marine Civil Engineering, College of Civil and Transportation Engineering, Shenzhen University, Shenzhen 518060, China. E-mail: xingf@szu.edu.cn

utilization,[15,16] water transportation,[17,18] vapor manipulation[19,20] and water collection.[21,22] In the early stage of solar evaporation, scientists paid a lot of attention to photothermal materials to pursue intensified interfacial evaporation.[23,24] However, the production of distilled water is not only governed by heat generation at the interface, but also relies on the coordination and cooperation of each functional component in the solar evaporation system. A typical structure of a solar evaporation system for freshwater production is illustrated in Fig. 1. Recent advances in this field have shifted to the system designs of functional modules, including thermal manipulation structures,[25] water transportation pathways,[11] and vapor condensation systems,[26] which aim to tackle the problems of energy dissipation,[27] salt crystallization,[28,29] and water yield[26] occurring in the solar evaporation process. These developments significantly promote the performance of solar distillation from different angles, thus maturing this green technology to a new stage.

To date, many reviews related to solar absorbing materials and specific applications have been reported. For example, reviews reported by Gao *et al.*[30,31] mainly focus on the investigation of photothermal materials and system designs for energy manipulation. The review reported by Dao *et al.*[32] only describes recent advances in carbon-based sunlight absorbers for solar-driven evaporation systems. Zhang *et al.*[33] presented a comprehensive review of photothermal-assisted applications, including distillation, sewage treatment, photocatalysis, and water harvesting from the air. Liu *et al.*[34] summarized and analyzed the critical processes involved in a solar desalination system with mathematical models, but without consideration of freshwater production. Comprehensive reviews considering the whole process of solar-driven evaporation have been published.[35,36] Nevertheless, these reviews have been mainly focused on photothermal effects and the structural architecture of the solar-driven evaporation system was not sufficiently discussed. Given the recent reported advances in system designs contributing to efficient energy harnessing, salt rejection, and water harvesting, it is thus time to systematically summarize the pros and cons of the technologies and map out guidelines for supporting the future development of clean water generation systems. Herein, we first present a mathematical model to quantitatively evaluate the system performance of solar distillation at different stages. Then, we demonstrate the significance and effects of energy input, water transportation, and vapor manipulation on the performance enhancement of individual stages in solar distillation. Next, we summarize the recent progress of applications based on solar-driven evaporation and discuss the underlying mechanism. Finally, a conclusion and remaining challenges in this field are presented.

2. Performance evaluation and calculation

A solar-driven evaporation system aims to produce freshwater using solar energy. In this process, the system firstly takes in solar energy, and then converts it into heat to vaporize water, followed by freshwater generation by condensation. Any stage in this process involves rather complex physical phenomena and energy changes. In short, the energy conversion and vapor generation mainly happen around the solar absorber, where the air–water interface is located. Taking a control volume enclosing the solar absorber, as shown in Fig. 2, and assuming a steady state, there are three major energy flows, namely solar radiation, heat loss, and mass flow of water/vapor, all three of which must remain in balance. Several metrics, including photothermal conversion efficiency, solar-to-steam efficiency, and water evaporation rate, have been proposed to evaluate the efficiency of energy utilization in the different stages. Efforts have been constantly devoted to improving the performance by maximizing these metrics. Interestingly, vapor condensation, as the final and most straightforward subprocess for freshwater production, has usually been neglected in performance evaluation. Each subprocess in the solar distillation exhibits unique features and functions, which play a critical role in the overall

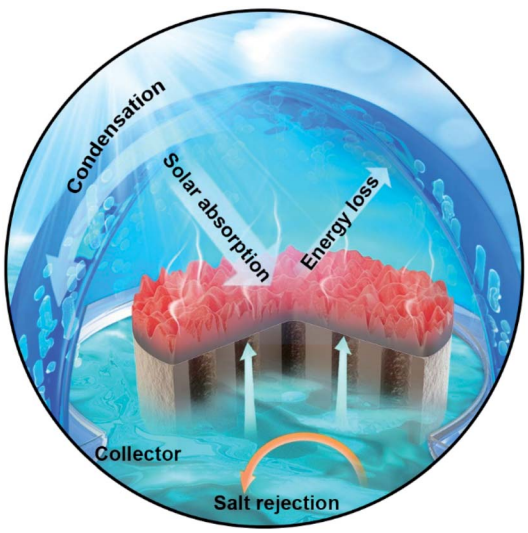

Fig. 1 Schematic of a solar evaporation system.

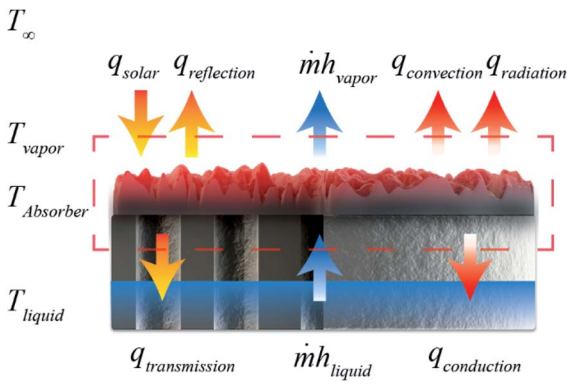

Fig. 2 The three major processes governing the energy balance of the control volume (boxed in red dashes), namely solar radiation, mass transport, and heat loss, indicated by arrows in orange, blue, and red, respectively. q, heat flux. $\dot{m}$, mass flow rate. h, enthalpy.

performance for freshwater production. In this section, performance evaluation methods for individual stages during solar evaporation are provided, aiming to clarify the corresponding underlying physical process and shed new insights on performance enhancement.

2.1 Solar–thermal conversion

Solar–thermal conversion is the initial stage of solar-driven evaporation, which lays the foundation for freshwater generation. In general, solar–thermal conversion comprises two parts: light harvesting and photothermal conversion. An understanding of these process is of great importance to enhancing the performance from the basic and motivating developments in exploring advanced system designs.

2.1.1 Light harvesting. The light harvesting ability of the solar absorber is the prerequisite for attaining efficient light to heat conversion. When solar radiation is incident upon the surface of the solar absorber, the irradiation may be reflected, transmitted, or absorbed. The absorption is the net energy inflow and can be expressed by

$$q_{\text{absorption}} = q_{\text{solar}} - q_{\text{reflection}} - q_{\text{transmission}} \quad (1)$$

The absorptivity of the solar absorber α is defined as the fraction of the solar radiation absorbed, reflectivity ρ is defined as the fraction reflected, and transmissivity τ is defined as the fraction transmitted. Solar radiation possesses a spectrum which resembles a 5778 K blackbody, with deviations mainly due to atmospheric absorption and scattering, and the majority of the irradiation energy lies in the ultraviolet (~3%), visible light (~45%), and infrared (~52%) bands with a wavelength in the range of 300 to 2500 nm.[37] As such, characterization of a material's absorption, reflectivity, and transmissivity is conducted in this wavelength range. Since solar absorptance is a measure of the ability of a photothermal module to harvest solar energy, it is determined by the ratio of the total acquired solar radiation to the incident radiation. Because most solar absorbers appear opaque in this wavelength region, the transmissivity is commonly near zero. Therefore, the absorptivity α can be experimentally determined by measuring the reflection at different wavelengths, following

$$\alpha = \frac{\int_{300\ \text{nm}}^{2500\ \text{nm}} [1 - \rho_\lambda(\lambda)] G_\lambda(\lambda) \mathrm{d}\lambda}{\int_{300\ \text{nm}}^{2500\ \text{nm}} G_\lambda(\lambda) \mathrm{d}\lambda} \quad (2)$$

where ρ_λ is the reflectivity and G_λ is the spectral irradiation, as a function of wavelength λ. Thus, the absorbed solar irradiation can be determined using

$$q_{\text{absorption}} = \alpha q_{\text{solar}} \quad (3)$$

High absorptivity is a property of a solar absorber that is critical to achieving optimal efficiency. As discussed in the following sections, owing to innovations in topographical and geometrical design, which significantly reduce the reflection, an absorptivity of over 95% has been able to be reached.

2.1.2 Photothermal conversion. Although light harvesting is a decisive ability for acquiring solar energy, the subsequent photothermal conversion is crucial to generate heat to vaporize water. This process requires a solar absorber to convert sunlight energy to thermal energy effectively, rather than undergo radiative re-emission.

Various nanomaterials, including inorganic[38,39] and organic materials,[40,41] have been exploited for solar-driven evaporation. To compare the performances between different materials, light-induced thermal generation is quantitatively analyzed with photothermal conversion efficiency. Conventionally, a direct experimental method to acquire photothermal conversion efficiency measures the temperature variation under an incoming light source. Typically, the solar absorber material is dispersed in the solution phase and a light source shone on it. The total mass, heat capacity, and light absorbance of the sample material, as well as the light intensity, as another important factor, are also taken into account to calculate the efficiency. With the same measurement of the container system, the photothermal conversion efficiency of the solar absorber material can be estimated. However, it is noteworthy that this method is typically used for single-wavelength light-to-heat conversion. For solar-driven evaporation, which occupies the whole spectrum of solar irradiation, it might be more reasonable to compare the thermal energy generation with the input solar energy within a defined period.

2.2 Water evaporation

In order to maximize the vaporization efficiency, the generated heat should be used entirely for the purpose of water evaporation. However, in practice, heat dissipation will inevitably consume thermal energy and undermine the evaporation efficiency. Thus, to control the thermal distribution during water evaporation, it is essential to take a look at the heat allocation. Herein, we summarize the critical factors that affect heat occupation and describe the physical processes with mathematical equations.

2.2.1 Heat dissipation. As the temperature of the solar absorber and water within the control volume is elevated above the surroundings, heat inevitably dissipates into the surroundings, resulting in energy loss. The heat transfer happens mainly by three routes: conduction into bulk water, convection into the surrounding air, and radiation into the surroundings. The conduction heat flux $q_{\text{conduction}}$ can be estimated with

$$q_{\text{conduction}} = \kappa \left.\frac{\partial T}{\partial x}\right|_{\text{border}} \quad (4)$$

where κ is the conductivity of water and $\left.\frac{\partial T}{\partial x}\right|_{\text{border}}$ is the temperature gradient at the border of the control volume, though estimating the temperature gradient is not a trivial task. The convection heat flux $q_{\text{convection}}$ can be estimated with

$$q_{\text{convection}} = h(T_{\text{PTM}} - T_\infty) \quad (5)$$

where h denotes the natural convection coefficient in a buoyancy-driven flow, which is dependent mainly on temperature

and surface dimension. h can be estimated using empirical equations and is normally in the order of ~1 W m^{-2} K.[42–44] The radiation heat flux can be calculated with

$$q_{\text{radiation}} = \varepsilon\sigma({T_{\text{PTM}}}^4 - {T_\infty}^4) \quad (6)$$

where ε is the emissivity of the solar absorber surface, σ is the Stefan–Boltzmann constant, and T_∞ the temperature of the surroundings.

Due to the empirical nature of heat flux calculation in general, the heat loss determined using these equations provides only a rough estimate. However, it offers important implications for strategies for the minimization of energy loss. For example, assuming the temperature of the solar absorber is 41 °C and of the surroundings is 27 °C, the conductive, convective, and radiative heat losses are ~2.3%, 3.0%, and ~4.0% of the solar energy,[43] suggesting that the three heat loss mechanisms make similar contributions.

2.2.2 Mass flow of water/vapor. Liquid water flows into the control volume at a temperature of T_{liquid} and an enthalpy of h_{liquid}, evaporates at the surface of the solar absorber, and flows out of the control volume as vapor at a temperature of T_{vapor} with an enthalpy of h_{vapor}. The enthalpy change, Δh, can be estimated by adding sensible heat and phase change enthalpies, following

$$\Delta h = h_{\text{vapor}} - h_{\text{liquid}} = c_{\text{p}}(T_{\text{vapor}} - T_{\text{liquid}}) + h_{\text{lg}} \quad (7)$$

where c_{p} is the specific heat and h_{lg} is the heat of evaporation at T_{vapor}, with the assumption that the dependence of c_{p} on temperature is negligible. However, we suggest that, whenever applicable, the enthalpy change should be calculated using experimentally measured thermodynamic properties from thermodynamic databases.

The mass flow rate is usually determined by continuously monitoring the weight change of the water using an analytical balance. However, it should be noted that under dark conditions, water also takes in heat from the surroundings and evaporates. As such, a proper control experiment should be performed, and the baseline mass flow rate generated under dark conditions should be subtracted.[10,45]

As we mentioned earlier in Section 2.1.2, the photothermal conversion efficiency of a solar absorber is difficult to calculate according to conventional methods. However, from a systematic point of view, such efficiency can be described as solar-to-steam conversion efficiency, which denotes the energy applied for water vaporization *versus* the total energy supplied. Briefly, solar–thermal conversion efficiency η is described as the fraction of the solar irradiance that has been utilized to generate vapor. It can be calculated following

$$\eta = \frac{\dot{m}\Delta h}{q_{\text{solar}}} \quad (8)$$

where $\dot{m}$ is the mass flow rate.

The evaporation rate, which is essentially the mass flow rate $\dot{m}$, characterizes the productivity of the vapor generation process. As discussed in the following sections, increasing the solar–thermal conversion efficiency and evaporation rate has been the goal of solar–thermal research. Currently, researchers have been able to achieve a thermal efficiency of up to 94%.[46] In an ideal case, water evaporates in an isothermal process with minimal enthalpy change, and solar energy is completely converted to the evaporation enthalpy of water. Under one sun illumination (1000 W m^{-2}) and assuming a water temperature of 25 °C, where Δh is roughly 2400 kJ kg^{-1}, the mass flow rate of the generated vapor is estimated to be 1.50 kg m^{-2} h^{-1}. This value can serve as a benchmark in the performance evaluation of endeavors in system design.

2.3 Vapor condensation

Desalinated water can be collected by condensing the generated vapor. By reducing the temperature of the vapor below the saturation temperature $T_{\text{sat.}}$, commonly known as the dew point, vapor condenses into liquid water. In general, condensation can happen in three ways: homogeneous condensation, where water droplets form within the vapor and result in a fog; direct contact condensation, where vapor comes into contact with liquid water and merges into it; and surface condensation, where vapor touches a cold surface and condensate forms on the surface. Due to its ease of implementation, surface condensation is the most commonly adopted method for water collection in solar stills.

Surface condensation can be initiated when vapor comes into contact with a surface with a temperature T_{surface} lower than $T_{\text{sat.}}$ and liquid nucleates on the surface. The condensation process is then driven by free convection of the vapor phase, and thus the geometry of the surface and the flow condition of the vapor phase have significant impacts on the effectiveness of the condensation. Latent heat is released and transferred to the surface, and the total heat transfer can be calculated from[42]

$$Q_{\text{condensation}} = h_{\text{condensation}}A_{\text{surface}}(T_{\text{sat.}} - T_{\text{surface}}) \quad (9)$$

where $h_{\text{condensation}}$ is the heat transfer coefficient due to condensation and A_{surface} is the area of the surface. $h_{\text{condensation}}$ represents the effectiveness of the heat transfer in the condensation process and can be estimated using empirical equations. Once the value of $hc_{\text{ondensation}}$ has been obtained, the mass flow rate of the condensate can be calculated from

$$\dot{m} = \frac{h_{\text{condensation}}A_{\text{surface}}\left(T_{\text{sat.}} - T_{\text{surface}}\right)}{\Delta h} \quad (10)$$

where Δh is the enthalpy difference between the saturated vapor and liquid water at T_{surface}. Therefore, to achieve optimal water production, the condensation heat transfer should be maximized. Eqn (10) implies four major strategies to increase $\dot{m}$: reducing Δh, increasing $h_{\text{condensation}}$ or A_{surface}, and increasing the difference between $T_{\text{sat.}}$ and T_{surface}.

Upon condensation on the surface, the condensate can form either a liquid film or drops, in processes termed film condensation or dropwise condensation, respectively, depending on the surface properties. In general, hydrophilic surfaces, such as glass surfaces, lead to film condensation, and hydrophobic surfaces, such as plastic surfaces, lead to dropwise

condensation. In either case, the condensate poses additional thermal resistance and thus hinders the heat transfer. In dropwise condensation, the condensate occupies less surface area, and the $h_{condensation}$ can be significantly larger than that in film condensation.[42] However, solar irradiation normally needs to pass through the condensation surface before reaching the photothermal materials in most solar stills, and drops generate significant reflection, drastically reducing the efficiency of solar absorption.[21] Therefore, it has been recommended that hydrophilic surfaces should be used for condensation in solar stills. The inclination of the surface can affect the retrieval of the condensate and its accumulation on the surface, thus also affecting $h_{condensation}$. So researchers have looked into the effect of inclination angle on vapor condensation.[21] In addition, active removal of the condensate from the surface by wiping or vibration has also been reported in an attempt to enhance the heat transfer.[47]

The efficacy of increasing $A_{surface}$ is straightforward and has indeed been confirmed in the effort to maximize condensate production.[22] Several methods have also been proposed to increase the difference between $T_{sat.}$ and $T_{surface}$. Essentially, any methods that increase solar absorption and water evaporation can boost the humidity within the chamber, which in turn increases $T_{sat.}$. Since vapor condensation releases latent heat onto the surface, heat must be effectively dissipated from the surface to the surroundings to prevent $T_{surface}$ from rising. To achieve this goal, measures such as cooling the surface and using a thinner surface to accelerate heat conduction have been tested.[48,49]

3. System designs for energy manipulation

Sunlight capture and photothermal generation are of great importance in solar-driven evaporation. In the past few years, numerous research works have been devoted to developing photothermal materials with broadband sunlight absorbance[32,50] and promising heat conversion efficiency.[51] Various types of novel materials, including plasmonic nanoparticles,[52–55] carbon-based materials,[56–62] MXene membranes,[38,63,64] and semiconductor nanomaterials,[65–67] have been studied and reformed to achieve efficient sunlight capture and thermal generation. Readers who are interested in the details of photothermal generation, materials selection, and materials design, can find more information in the review by Gao *et al.*[31] Currently the performance of photothermal conversion is approaching a ceiling. In order to further pursue the water evaporation rate in solar evaporation systems, the research focus is gradually shifting to system designs with sophisticated energy management from materials investigations.[68–71] Under the assumption of excellent heat conversion efficiency, several strategies are proposed that can be employed for the judicious design of solar evaporation systems endowed with superior energy utilization, including (1) strengthening sunlight capture with a modified surface topography; (2) increasing thermal accumulation by a concentration scheme; (3) recovering additional energy from the environment, and (4) reducing the enthalpy change of evaporation, as shown in Fig. 3. The following sections will discuss the proposed strategies in detail to demonstrate the relationship between system design and energy manipulation.

3.1 Modification of surface topography

In the past few years, great progress has been made in developing interfacial solar evaporators with promising light absorption (covering the entire solar spectrum)[72] and remarkable photothermal efficiency.[33] Although higher energy utilization efficiency has been realized, compared to the volumetric system, membrane-based interfacial solar evaporators still suffer from significant optical and energy losses,[14,73,74] regardless of the light-absorbing properties of the photothermal materials. Such losses originate from diffuse reflectance and thermal radiation, which compromise the energy influx and

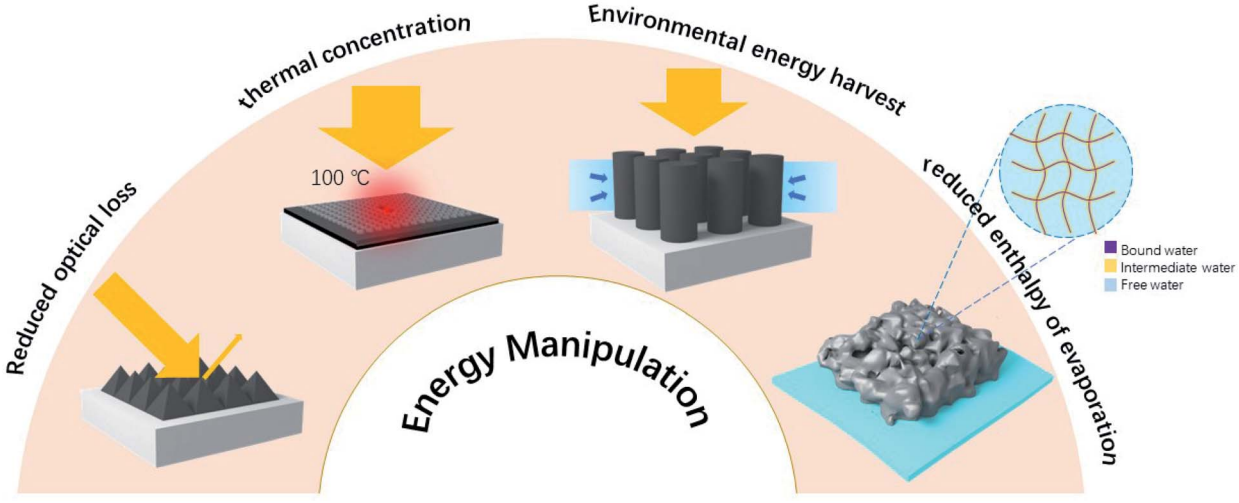

Fig. 3 A schematic demonstration of energy manipulation strategies.

water evaporation. Moreover, in practical conditions, the changes in solar angle might be another issue to affect solar absorbance and vapor production.[12] Hence, to address the aforementioned challenges, solar evaporators with a designed surface topography have been emerging in recent years.

3.1.1 Enhanced light absorption by multiple reflections. One of the early solutions which aimed to recover the dissipated light energy and thermal energy was proposed by Shi and co-workers, who created a cup-shaped solar absorber to reduce energy loss.[16] The reflected energy from the evaporator basin can be efficiently reabsorbed by multiple reflections, providing extra energy for heat generation. Specifically, a maximum evaporation rate of 2.04 kg m^{-2} h^{-1} was achieved under one sun irradiation with an optimal cup structure, and such a value was far higher than that of a 2D planar system (1.21 kg m^{-2} h^{-1}). A similar strategy which aims to recover the reflected sunlight was introduced by Xu *et al.*, who designed an origami solar absorber made of pencil-drawn paper.[75] Compared to a planar system, the origami system with a folded angle of 90° has a 41% larger surface area, which is beneficial for solar absorption and water evaporation. In a field experiment, the distillate productivity of the origami system was 22% higher than that of a planar system, owing to the reabsorption of dissipated sunlight. Wang and co-workers fabricated an artificial 3D cone composed of a polypyrrole (PPy)-coated polyvinylidene fluoride (PVDF) membrane to study the structure–energy nexus.[76] As shown in Fig. 4a, a series of samples with tunable apex angles (180°, 121°, 86°, 70°, and 56°) were prepared to investigate the effect of the opening angles on photothermal performance. Owing to the structure-dependent optical properties, the surface temperature increased as the apex angle became smaller. A maximized solar evaporation rate of 1.70 kg m^{-2} h^{-1} was achieved with the optimized cone apex angle, which was nearly 1.7 times higher than that of the corresponding planar system.

The complexity of the surface structure of solar absorbers was proved to be effective in influencing multiple reflections. Another origami-type solar evaporator with a flower-like surface topography was designed by Li and co-workers.[77] According to Fig. 4b, origami structures with individual folding structures (AF-0F, 4F, 8F, 16F, and Origami Rose) were prepared to demonstrate the light–matter interaction. It was found that the number of petals and the depth of the folded area are both critical to the overall light absorption and water evaporation rate. Hence, the Origami Rose sample, with the most petals and the deepest depth can afford the most rounds of light reflections, exhibiting the highest optical absorption of 99% and water evaporation rate of 2.12 kg m^{-2} h^{-1} under one sun irradiation. However, it is worth mentioning that, even though the Origami Rose possessed the best energy utilization in this work, the surface temperature was much lower than that of the planar PPy disk during the solar evaporation experiments. Such a finding may contradict the previous concept that a higher

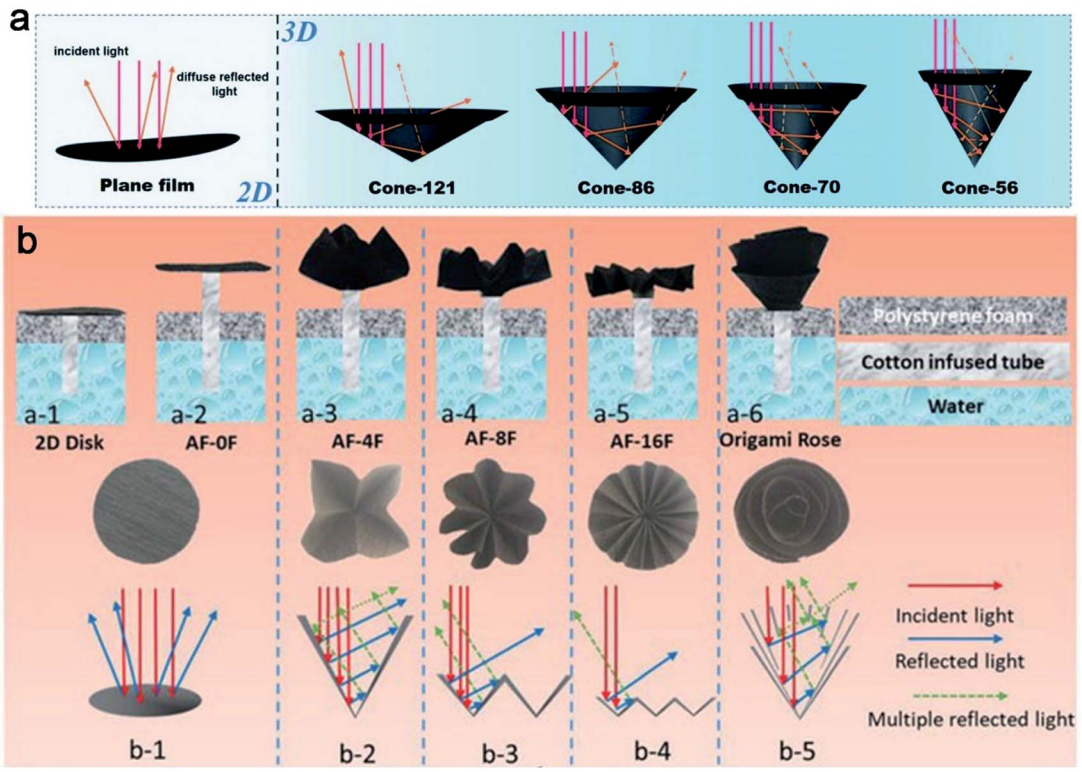

Fig. 4 Schematic of energy recovery by a solar evaporation system with a designed surface topography. (a) Artificial 3D cone-shaped structure. Reproduced with permission.[70] Copyright 2018, Royal Society of Chemistry. An isolation PPy-based origami solar evaporation system with flower-like surface topography. (b) A schematic of the structure of solar evaporation systems and the light–matter interaction. Reproduced with permission.[71] Copyright 2018, Wiley-VCH.

surface temperature can induce stronger water evaporation. According to the authors, the enlarged surface area of the Origami Rose can afford extensive evaporation, hence giving rise to lower thermal accumulation than that in the planar device. Furthermore, a low surface temperature was also beneficial for reducing the radiative energy loss and improving the energy utilization efficiency.

By modifying the surface topography of the solar absorber, the performance of solar evaporation is hugely improved due to the enhanced sunlight capture, stronger heat generation, and enlarged evaporation area. Currently, the design of the surface structures of solar absorbers plays a more significant role in performance enhancement than materials investigation. However, there are still many issues that need to be solved. For example, although more dissipated energy can be reabsorbed with the increase in height of the sidewall and consequently generate a higher temperature, the solar absorber may afford greater inner humidity and hence inhibit vapor production. In this case, the sustainability of the solar-driven evaporation device may be greatly hindered. Hence, there is still much room for further modification.

3.1.2 The evaporation of solar absorbers with a matrix form. It is clear that surface topography is crucial for efficient solar energy utilization. The previous examples demonstrate the effect of multiple reflections and evaporation areas on the overall performance of vapor production on a single unit. In a more practical situation, a matrix of evaporation units is required for large-scale freshwater generation.

Hong and co-workers reported an origami-type solar evaporation system with a surface structure of periodic pleats.[78] As indicated in Fig. 5a, the periodic surface structure contains repeated units with valleys and peaks, composed of four parallelogram faces. With increasing surface areal density ($A_{active}/A_{project}$: the ratio of the evaporation area to the projection area), vapor production was increased due to the enhanced light capture and heat loss recovery. With the optimal areal density of 4.65, nearly 100% of solar energy efficiency was absorbed with an evaporation rate of 1.59 kg m^{-2} h^{-1}, which was nearly 50% higher than that of the planar system. To obtain more insight into the energy utilization phenomenon, an infrared camera was used to capture the temperature distribution in the origami system during the evaporation experiments. An inhomogeneous spatial temperature distribution was observed across the proposed origami periodic surface. As shown in Fig. 5b, with and without sunlight illumination, the valley folds always exhibit a higher temperature than the mountain folds in a wet state. Such a phenomenon can be explained by the stronger water evaporation on the mountain fold. In addition, due to the temperature gradient on each unit cell, thermal energy can be further re-utilized due to the heat flux from the bottom to the top. Thus, both the reduced light reflection by the concave structure and the inverse heat flux resulted in promising energy utilization. A similar isolation solar evaporation device made of PPy-functionalized cellulose paper with tunable microstructures and macroscopic geometries was proposed by Ni and his co-workers.[15] By folding the PPy-paper into a 3D "cootie-catcher-shaped" structure, a water evaporation rate of 2.99 kg m^{-2} h^{-1} was achieved under 1 sun irradiation, far exceeding the value (1.47 kg m^{-2} h^{-1}) of the 2D device.

A periodic undulating surface structure can also be seen in nature. Sun *et al.* used carbonized sunflower heads to achieve efficient solar vapor generation.[79] As shown in Fig. 5c, owing to the numerous 3D cavities on the top surface, solar energy can be absorbed extensively with minimized diffuse energy reflectance and thermal radiation. In addition, the hugely enlarged evaporation area was beneficial for water evaporation. Due to the structural features, a solar evaporation rate of 1.51 kg m^{-2} h^{-1} and an evaporation efficiency of 100.4% was achieved under one sun illumination (Fig. 5d). In contrast, carbonized sunflower head without the top bracts gave a much-reduced solar evaporation rate of 1.18 kg m^{-2} h^{-1} and evaporation efficiency of 78.4%.

In practical applications of solar evaporation, it is very important to consider the matrix form of the solar absorbers. It is believed that the density and shape of the solar absorber unit may hugely affect light absorption and vapor generation. However, as far as we are concerned, there has been no research study investigating and comparing the overall performance of solar-driven evaporation systems in unit and matrix forms. We may still acquire some insights from the research works mentioned above. For example, Hong's work indicated the relationship between surface areal density and vapor generation rate, which may provide a rough direction for the future development of a solar evaporation system with a matrix form.

3.1.3 Compensation for the incident angle effect. Although great progress has been made to achieve smart energy management and efficient water evaporation in the lab, performing solar vapor generation in an outdoor environment is quite different and more parameters need to be considered.

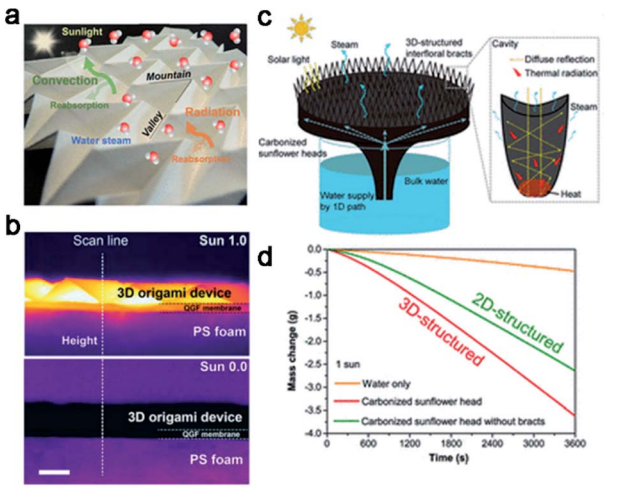

Fig. 5 (a) A solar evaporation system with a surface structure of periodic pleats. (b) The temperature distribution of a 3D origami device with/without 1 sun irradiation. Reproduced with permission.[72] Copyright 2018, American Chemical Society. (c) A solar evaporation system made of carbonized sunflower heads. (d) The water evaporating performance of carbonized sunflower heads. Reproduced with permission.[73] Copyright 2020, American Chemical Society.

One of the most significant issues in the practical experiment is the unstable sunlight intensity. In a laboratory experiment, solar vapor devices are always perpendicularly illuminated by simulated sunlight with a stable intensity of 1 kW m^{-1}. However, in practical outdoor conditions, the sun moves through the sky with changing elevation angles throughout the day. In most cases, only 50–90% of sunlight could arrive at the solar receiver surface, depending on the weather conditions (nearly 10–20% of energy diffusion occurs on sunny days and 50% occurs on cloudy days).[12] Moreover, the randomly moving clouds would occasionally block the sunlight. In this case, there is little chance for a solar evaporation system to operate at its full potential.

An umbrella-shaped evaporation device made of graphene oxide film was designed by Li *et al.*[80] As shown in Fig. 6a, due to the promising light absorption of the graphene oxide and the umbrella-shaped morphology, the proposed 3D device can acquire sunlight from different incident angles. In a field experiment, nearly 24% enhancement of sunlight absorption was realized by the umbrella-shaped device, resulting in 1.43 times higher vapor generation than the planar device. Similar work has been reported by Chen and co-workers.[12] In order to compensate for the varied solar elevation angles, a 3D hemispherical solar-driven evaporation device was designed. As shown in Fig. 6b and c, a high ratio of solar energy input is achieved by the 3D hemispherical device with solar elevation angles varying from 0 to 90 degrees. In order to simulate outdoor conditions, 2D planar, cylindrical, and 3D hemispherical devices were irradiated with wide incident angles (90°, 80°, and 65°) under moderate intensity (0.75 sun). The experimental results demonstrated that the water evaporation rate and energy efficiency of the 3D hemispherical device remained constant while the performance of the other two systems was downgraded drastically with decreasing incident angle. The hemispherical surface was capable of maintaining the highest solar energy input from 0° to 90°, and showed promising potential to prolong the working period throughout the day. Moreover, the hemispherical structure exhibits the best performance in coping with the variation in solar angles in both indoor and outdoor experiments. After 3 h of sunlight illumination in field experiments, a solar evaporation rate of 4.83 kg m^{-2} was obtained by the 3D hemispherical system, which was 15.8% higher than that of the cylindrical system (4.17 kg m^{-2}) and 50.5% higher than that of the 2D planar system (3.21 kg m^{-2}).

Nature already provides an elegant solution for efficient solar vapor generation. In recent years, carbonized biomasses have received especial attention in solar vapor generation, due to their intrinsic surface structure for light trapping, fast water evaporation, thermal loss reduction, efficient water transportation, and good scalability. Bian and co-workers introduced a highly efficient solar evaporation system made of carbonized tree-like furry magnolia fruit.[81] As indicated in Fig. 6d, owing to the unique surface structure, which is composed of numbers of carpels, multiple sunlight reflections occurred, which efficiently recovered and recycled the incident solar energy, resulting in ~98.5% solar utilization efficiency. In addition, the large surface area and additional available free space (offered by the staggered pod-like carpels) afforded fast vapor escape with reduced vaporization enthalpy, which boosted the vapor production throughout the day. Hence, an impressive solar vapor generation rate of 1.22 kg m^{-2} h^{-1} in the dark and 3.15 kg m^{-2} h^{-1} under 1 sun irradiation was achieved. Similar to the 3D hemispherical system mentioned previously, the tree-like isolation solar evaporation system can also collect more sunlight throughout the day than a 2D planar system. In an

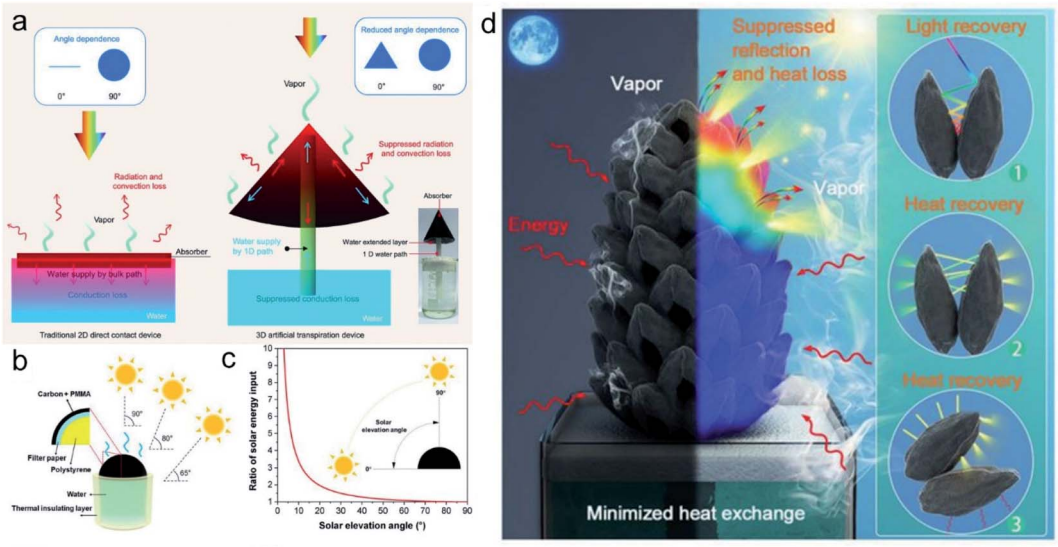

Fig. 6 Several isolation solar evaporation systems with designed surface topography for offsetting the angle of the incidence effect. (a) An umbrella-shaped system. Reproduced with permission.[74] Copyright 2017, Oxford University Press. (b) A hemispheric-shaped system and (c) its performance coping with varied light incident angles. Reproduced with permission.[12] Copyright 2020, American Chemical Society. (d) The carbonized tree-like furry magnolia fruit. Reproduced with permission.[75] Copyright 2019, Wiley-VCH.

outdoor experiment (from 7:00 a.m. to 6:00 p.m.), a remarkable vapor production rate of 15.6 kg m^{-2} was obtained by the tree-like system, far succeeding that (4.2 kg m^{-2}) of a 2D evaporator with the same ground area.

Previously mentioned designs compensated for the variation in solar angles by always making sure that the surface of the solar absorbers can be shone on by the sun. However, it is impossible to absorb the solar energy maximally throughout the day. In contrast to passively compensating for the solar absorption loss with pre-designed surface structures, Qian *et al.*[82] developed an artificial phototropism (a sunflower-life biomimetic omnidirectional tracker, SunBOT) for omnidirectional light harvesting. The proposed SunBOT system is composed of nanostructured thermal stimuli-responsive polymers and photothermal nano-agents. Similar to the biological asymmetric growth of plants under light exposure, the SunBOT is able to bend towards a light source due to the asymmetric deformation between the illuminated high-temperature region and the un-exposed low-temperature region. The tropistic locomotion of SunBOT was further applied in a solar evaporation system. An array of SunBOTs can accurately respond and turn toward the light source. In this case, the incident energy loss is hugely recovered with up to 400% enhancement in solar evaporation in an operation window of 164° (−82 to 82°), compared to a non-tropistic surface.

It is of great significance to overcome the variation in solar angles in practical applications. The early trials mostly relied on the structural features of solar absorbers; however, this inevitably left some surfaces in shadow, which undermined the full potential of solar-driven evaporation. Recently, solar absorbers with the ability to chase and face the light source have been reported. Such designs may significantly improve the solar evaporation performance by achieving maximum sunlight absorption throughout the day. However, such designs are still in their infancy, and the proposed structures may be too fragile to be applied in practical situations. Hence, further improvement in the structural designs of solar absorbers is required to achieve higher energy manipulation efficiency.

3.2 Energy concentration scheme

Solar–thermal technology, which converts solar energy into thermal energy, was extensively constructed for industrial activities a few decades ago. In the typical design of a solar–thermal plant, a solar concentrator, solar energy receiver and heat-transfer fluid were included. With solar tracking and concentrating functions, the power of light energy can be intensified as high as 1000 fold with an operating temperature over 400 °C.[83] Although the conventional-thermal technology was only used in industrial electricity generation, the heating mechanism could also have a new impact on solar vapor generation.

In the field of solar vapor generation, with the enhanced power density of simulated solar light, a hugely improved water evaporation rate has been achieved by interfacial systems. Zhu and co-workers combined plasmonic nanoparticles with carbonized wood[62] to achieve highly efficient solar vapor generation under concentrated incident light. Specifically, under 10 suns of illumination, a water evaporation rate of 11.8 kg m^{-2} h^{-1} was accomplished, far above the reported value under one sun. Mu and co-workers[11] fabricated carbon aerogel consisting of hollow carbon nanotubes to achieve an evaporation rate of ~4.2 kg m^{-2} h^{-1} under 3 suns with a surface temperature of 54.6 °C. Such values were much higher than those (~1.44 kg m^{-2} h^{-1} water evaporation rate and 40.5 °C surface temperature) under 1 sun. Yang and co-workers prepared a photothermal membrane composed of single-wall carbon nanotubes and MoS_2 films.[39] The proposed membrane exhibited 6.6 kg m^{-2} h^{-1} water evaporation rate and 106 °C surface temperature, under 5 suns of irradiation.

Without a doubt, the overall water evaporation rate is positively correlated with the total energy received by the system. With more solar energy absorbed, more thermal energy is generated, resulting in a dramatically enhanced water evaporation rate. However, in practical conditions, integrating an optical concentrating component (US$200 per m) will be a huge burden on the fabrication and maintenance costs. Hence, an energy concentration scheme with a facile preparation process is highly desirable for efficient solar evaporation.

In order to address this challenge, Ni and co-workers provided a novel strategy which can thermalize a floating solar receiver to 100 °C in an ambient environment without a light concentrator.[44] The typical structure of the solar evaporator is shown in Fig. 7a, in which the photothermal material is surrounded by heat insulation layers with a middle-drilled channel. In this case, the generated heat can be localized in the confined area and concentrated for water vaporization. The specific material compositions and device structure are indicated in Fig. 7b. Although the top bubble-wrap layer partially (~20%) reduced the solar influx, the convective heat loss driven by the solar–thermal process was also hugely diminished. As shown in Fig. 7c, under one sun illumination, a maximum vapor temperature of 98 °C is achieved with the thermal concentration C_{therm} (the ratio of the illumination area to the evaporation area) of 1300×. Such a high temperature contributed to the heat localization and thermal concentration strategy. The practical performance of this solar vapor system was evaluated in an outdoor environment. As shown in Fig. 7d, remarkably, even with a varying solar flux (~200–1000 W m^{-2}) and wind speed, the solar vapor system was able to recover its peak operating temperature (>95 °C) within minutes. Moreover, according to the simulation results, big tolerances to the properties of the top covering and solar influx were observed, making the proposed solar vapor system operable in diverse weather conditions. Generally, the strategy proposed herein significantly reduces the energy losses and accumulates thermal energy for intensified vaporization, providing a new insight into solar energy utilization. A similar structural design with an energy concentration capability at the evaporation front has been fabricated by Guo and co-workers.[25] The solar evaporation device was composed of a PVA hydrogel top layer and activated carbon paper as the photothermal bottom layer. With a tailored surface topography on the PVA layer, increased solar energy was harvested and consequently generated a higher

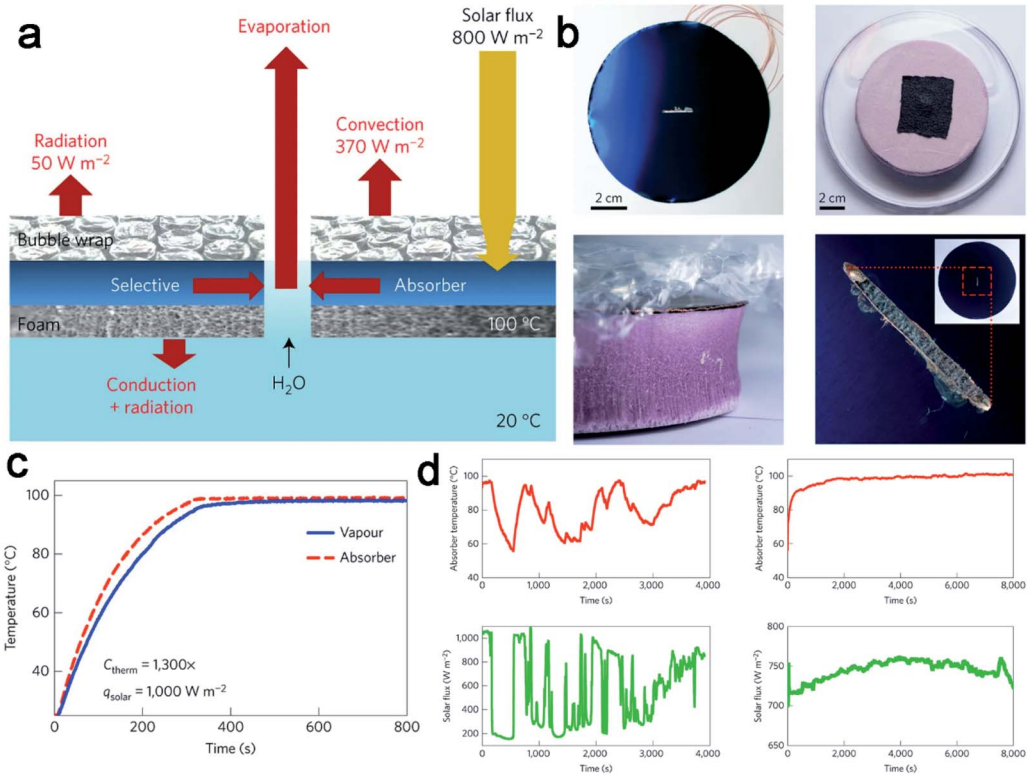

Fig. 7 (a) Schematic of energy flow on a solar water evaporator. (b) The components of a solar water evaporator. The performance of a solar water evaporator in (c) indoor experiments and (d) outdoor experiments. Reproduced with permission.[42] Copyright 2016, Springer Nature.

temperature for water evaporation. Strikingly, a water evaporation rate of ~2.6 kg m^{-2} h^{-1} and solar energy efficiency of ~91% were achieved under only one sun irradiation.

3.3 Energy recovery from the surroundings

In the previous sections, efforts devoted to enhancing the water evaporation rate by improving solar light absorption and applying thermal management were discussed. Those methods required an elaborated surface topography[81] or an enlarged evaporation area[84] to accelerate the water–vapor phase transition. Although considerable progress has been made to minimize the heat loss from the photothermal components in the past few years, the theoretical limit of water evaporation rate (based on the fixed solar energy input per unit area) is a huge roadblock impeding further development.[34]

In order to overcome these natural limitation, Song and co-workers discovered a new mechanism to boost water evaporation by generating cold vapor below room temperature.[85] Unlike the thermal confinement strategy mentioned previously, the authors actively ameliorated the effect of the heat insulator in order to enhance the heat exchange of the solar evaporator with the ambient environment. Under low-density solar illumination (0.2 sun), a low surface temperature (below room temperature) and a high evaporation rate (higher than the theoretical limit under the same solar input) were achieved. According to the authors, the increment in water evaporation originated from additional energy absorption from the warmer environment. When the temperature of the evaporator was higher than the ambient with a high-density solar flux (0.6 sun), environmental energy was no longer available to the evaporator, and hence could not be absorbed to promote the water evaporation rate. In order to implement this strategy under 1 sun irradiation, solar evaporators with enlarged surface areas and apex angles were prepared. As indicated in Fig. 8a, with an optimal apex angle of ~22.4°, an evaporation rate of 2.20 kg m^{-2} h^{-1} was accomplished under 1 sun illumination. Certainly, absorbing energy from the warmer environment provided a novel solution to going beyond the theoretical limits of solar-driven water evaporation.

A similar finding was reported by Li and co-workers,[86] who fabricated a smart solar evaporator, which can absorb solar energy and gain environmental energy simultaneously. The solar evaporation system was composed of an array of cylindrical columns, which were constructed from a cotton core and carbon nanoparticle decorated cellulose warps. As shown in Fig. 8b and c, under simulated sunlight irradiation, the top surface can efficiently absorb solar energy and generate heat; meanwhile, the side surfaces with a low temperature can absorb energy from the environment. Hence, a highly enhanced water evaporation rate was achieved by this system, far succeeding the corresponding theoretical limits at various light intensities.

Tu *et al.*[87] prepared a plug-in-type black nylon fiber (BNF) flocking boards system with an evaporation rate of 2.09 kg m^{-2} h^{-1} under 1 sun irradiation. With the combined effects of photothermal phenomenon and cold vapor generation, the water evaporation performance was well above the

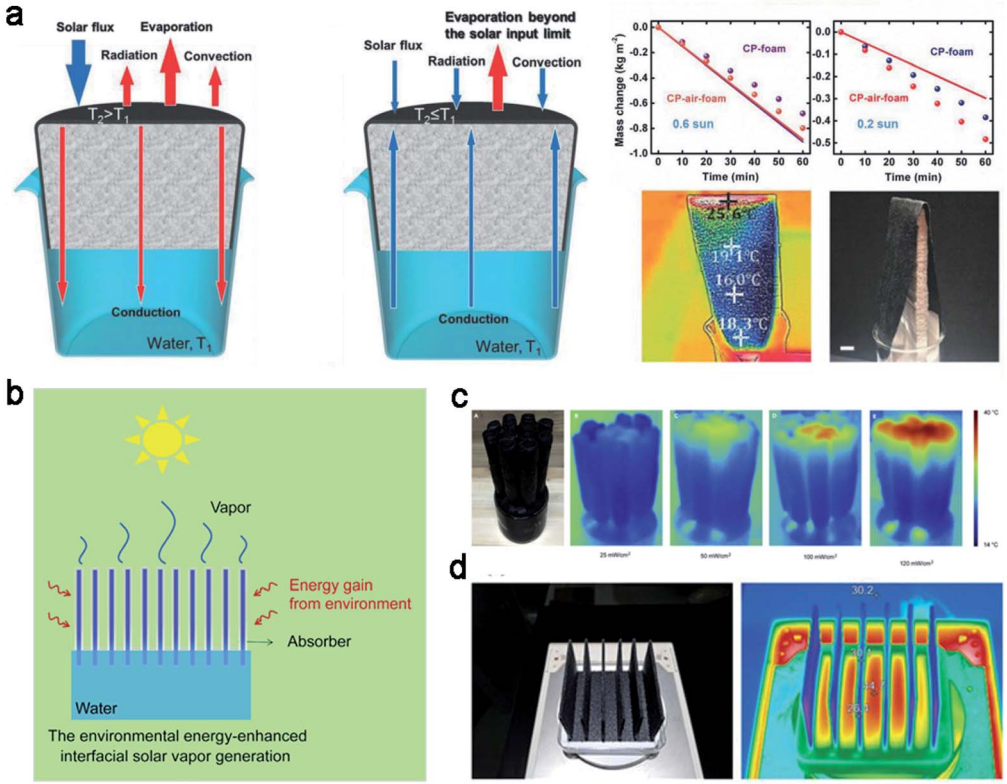

Fig. 8 Environmental energy-harvesting evaporators. (a) Energy flow of carbon paper on polystyrene foam under strong light illumination and low light illumination or in darkness; the performances of the prepared solar evaporator device with unique configuration under different solar intensities are demonstrated. Reproduced under the terms and conditions of the CC BY 4.0 License.[79] Copyright 2018, Wiley-VCH. (b) The energy flow of solar evaporation system composed of an array of cylindrical columns. (c) The temperature distribution of cylindrical evaporation system under different light intensities. Reproduced with permission.[80] Copyright 2018, Elsevier. (d) The configuration and temperature distribution of a plug-in-type black nylon fiber (BNF) flocking boards system. Reproduced with permission.[81] Copyright 2019, Wiley-VCH.

corresponding upper limit of 1.50 kg m^{-2} h^{-1}. The previously mentioned research work reported by Bian *et al.*[81] also utilized this strategy, gaining energy from the environment. As shown in Fig. 8d, the carbonized magnolia fruit always had a lower side surface (bottom part) temperature than the surrounding environment under solar irradiation. Such a condition was attributed to strong natural vapor production, which was also beneficial for gaining energy from the warmer environment. Hence, an extremely high evaporation rate of 3.15 kg m^{-2} h^{-1} under 1 sun illumination was obtained in their work.

Although the integration of environmental energy absorption efficiently increased the system input for vapor production and generated a water evaporation rate far beyond the theoretical limits, a new scientific question for cold vapor condensation for freshwater collection was introduced. It is challenging to release the thermal energy from cold vapor, when the temperature is below room temperature, using a conventional condensation method. Thus, there is a long way to go to optimize freshwater generation by gaining environmental energy.

3.4 Reduced enthalpy of evaporation

As mentioned in the above sections, much effort has been devoted to improving the solar evaporation rate through enhancing sunlight absorbance and energy manipulation by architectural design. Actually, the vapour production rate ($\dot{m}$) is determined by $\dot{m} = \eta^* q_{solar}/\Delta h$, where $\eta^* q_{solar}$ is the absorbed solar energy and Δh corresponds to the specific enthalpy change of liquid water to vapor. Apart from increasing the energy input for water evaporation, it has been found that the regulation of enthalpy is a powerful strategy to strengthen vapor production. The enthalpy of vaporization is the amount of energy required to induce the phase transition from liquid water to vapour. With a constant enthalpy of water evaporation (2444 J g^{-1}) and 1 sun irradiation, operating at the theoretical optimum, a conventional planar solar evaporator can only generate vapour at 1.47 kg m^{-2} h^{-1}. Hence, the reduction of enthalpy is considered a promising way to overstep the theoretical upper limit of water evaporation.

Recent advances have been reported in materials science methods to adjust the enthalpy of water evaporation. The water state in a hydrogel network has been manipulated to affect water evaporation. Due to the water-solubilizing groups in polymer chains, such as hydroxyl groups, amino groups, carboxylic groups, and sulfonic acid groups, water molecules can bond with polymers with noncovalent interactions, such as hydrogen bonding and electrostatic interaction.[88] As reported by Yu's group,[23] three types of water states, bound water,

intermediate water, and free water, have been found in water-filled polymeric structures. Among these, intermediate water, which exists between free and bound water, requires the least energy to be activated for evaporation. Hence, a photothermal hydrogel with higher degradation of crosslinking exhibited a strong solar evaporation effect. Specifically, with the optimal inner structure, a PVA hydrogel (loaded with PPy) required less energy demand for water evaporation, which was ~1400 J g^{-1}. Accordingly, a record high evaporation rate of 3.2 kg m^{-2} h^{-1} was achieved. In addition, the enthalpy can be further tailored by designing the architecture of polymer networks. According to Zhou *et al.*,[89] the introduction of chitosan can further reduce the energy demand of water evaporation, due to the co-existence of amine groups and an increased amount of intermediate water. Hence, a water evaporation rate of 3.6 kg m^{-2} h^{-1} was achieved by a chitosan/PVA hydrogel (loaded with Pyy). Inspired by the reduced enthalpy of chitosan/PVA hydrogel, Guan and his co-workers[164] applied bacterial cellulose (BC) to achieve a high proportion of intermediate water. Due to the ultrafine 3D cellulose network of BC, 69% of intermediate water was observed in BC hydrogels, resulting in a greatly reduced enthalpy of 997 J g^{-1}. Attributed to designs with reduced enthalpy and energy management, a water evaporation rate of 2.9 kg m^{-2} h^{-1} was achieved.

A reduced phase transition enthalpy has also been found in a surface-burnt wood sample. According to Tang *et al.*,[90] by regulating the hydrophilicity of surface-burnt wood and adjusting the height of the wood above a water surface, the enthalpy of water evaporation in wood can be reduced from 2444 to 1769 J g^{-1}. Such an enthalpy change was mainly attributed to the state transition of water from "gravity state" to "capillary state". In such a case, the microchannels of the wood were not blocked by water but were dredged with transpiration, resulting in much more evaporation space. In addition, during water evaporation, vapour was formed in single molecules or clusters consisting of a few to tens of molecules. Less energy was required for water clusters to escape from bulk water than for single molecules. Hence, due to the reduced enthalpy of 1769 J g^{-1}, a high evaporation rate of 1.93 kg m^{-2} h^{-1} under one sun irradiation was achieved by the wood-based evaporator.

In a real-world scenario, diffuse natural sunlight may not meet the energy requirements for efficient water evaporation. Hence, it is anticipated that developing new materials with a lower energy demand for water evaporation will be a promising approach to achieve rapid solar distillation under natural sunlight. Reducing the enthalpy of evaporation has, no doubt, shed new light on such a goal.

4. System designs for water transportation

Regardless of the progress achieved in optical and thermal energy management, liquid transportation[91] is another important issue affecting the overall solar evaporation performance. Although radiant heat can be reduced through surface structural designs and temperature control, as mentioned in the last section, water transportation from bulk water to the evaporation surface, taking most of the thermal energy, is considered to be the major heat-draining pathway. Hence, reducing the water convection loss is of great importance to achieving high energy efficiency and water evaporation rate.[92,93] Furthermore, in continuous and long-term operation, a fact that cannot be ignored is that the escape of a large amount of water vapor may be accompanied with the accumulation of salt crystals in the evaporation system.[62,94] The solid crystals not only clog the water and vapor transportation pathways[95–97] but also reflect sunlight[98] and reduce the solar input, resulting in a deterioration in freshwater productivity. Recent progress in solar water evaporation has explored various liquid manipulation schemes, which are feasible for limiting the heat convection loss to bulk water and repelling a high concentration of salt back beneath the water body.

4.1 Reduced thermal loss

From the structural point of view, water transportation is realized by an individual sub-component of the solar evaporation system. Such a component could be integrated[99,100] in the system as a complete unit or fabricated as a separate part.[101–103] Under sunlight irradiation, water is efficiently drawn into the photothermal area for evaporation. Inevitably, thermal energy will flow from the high-temperature surface to the low-temperature water, resulting in energy transfer, which provides water for the liquid–gas phase transition, or causes an unnecessary energy loss to the water body. Hence, in order to achieve the full potential of solar-induced thermal energy, the design of water transportation is critical. Theoretically, a good balance between vapor production and water transportation is beneficial for efficient thermal energy utilization.

4.1.1 Manipulation of water transportation pathway. Conventionally, in most cases, the water transportation pathway is integrated with a thermal generating layer or self-floating substrate.[104–106] To avoid direct contact with bulk water, Zhu *et al.*[62] prepared plasmonic wood (as depicted in Fig. 9a) which combined the merits of photothermal nanoparticles and a natural wood block for solar vapor generation. The internal hierarchical structure can efficiently pump water to the photothermal layer through the capillary effect. Although a high light absorption of 98% was achieved by the plasmonic wood, 30.6 °C surface temperature and less than 70% of solar energy efficiency were observed under one sun irradiation. Although carbonized biomass exhibits great promise in terms of low-cost fabrication and fast production, the water transported to the photothermal layer might far outweigh the needs for vapor production. The excess water supply might induce rapid water circulation, resulting in intensified heat exchange and heat loss. To ameliorate the heat convection to water and simultaneously maintain a sufficient water supply for vapor production, water transportation with fine manipulation is required.

Zhao *et al.*[23] created hierarchically nanostructured gels composed of polyvinyl alcohol (PVA) and polypyrrole (PPy) to investigate and pursue an optimal water transportation scheme.

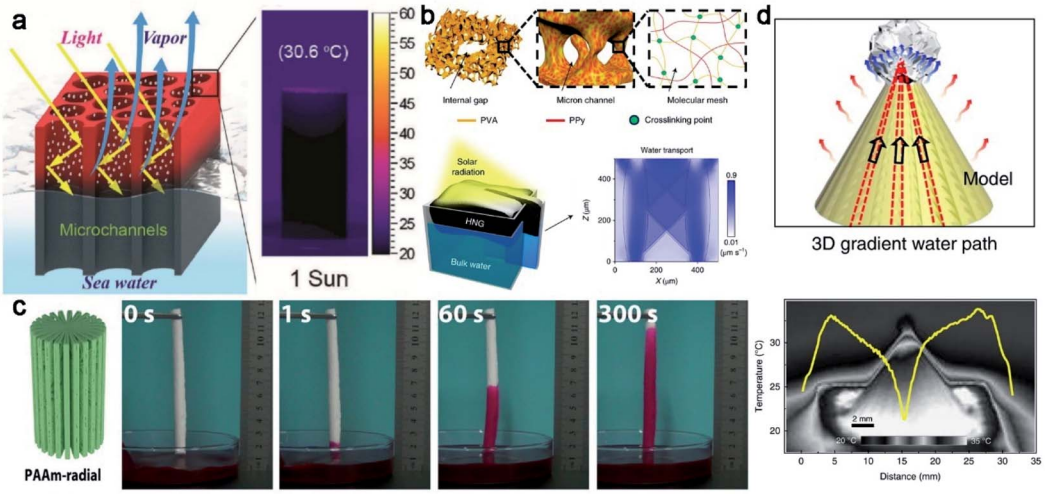

Fig. 9 Water transportation manipulated by: (a) plasmonic wood. Reproduced with permission.[56] Copyright 2018. Wiley-VCH. (b) Hierarchical PVA-based gel. Reproduced with permission.[23] Copyright 2018. Springer Nature. (c) Hierarchical PAAm-based aerogel. Reproduced with permission.[98] Copyright 2019. American Chemical Society. (d) Reversed cone-shaped structures. Reproduced with permission.[29] Copyright 2020. Springer Nature.

With varying weight ratios of PPy, PVA, and water, the inner structure of the gel device changed dramatically, which was critical for efficient water replenishment. With the optimized gel inner structure, composed of internal gaps, micron channels, and molecular meshes (as shown in Fig. 9b), a remarkable water evaporation rate of 3.2 kg m^{-2} h^{-1} under 1 sun illumination was achieved. In addition, the simulation results demonstrated similar water flow speed across the hierarchical gel, with 0.9 μm s^{-1} of bottom water replenishment lost 0.89 μm s^{-1} of top surface water. In this case, an energy efficiency of 94% was achieved. Moreover, besides the efficient water replenishment, such a remarkable water evaporation rate might also be attributed to the reduced vaporization enthalpy of water confined in gel meshes. A similar hierarchical structure was accomplished by Xu *et al.*,[107] who were inspired by conifer tracheid construction and fabricated an efficient water transportation and evaporation system with a polyacrylamide (PAAm)-based aerogel. With a well-defined inner structure, composed of radially aligned channels, micro pores, and molecular meshes, long-distance (>28 cm at 190 min) and rapid (>1 cm at 1 s and >9 cm at 300 s) antigravity water transportation was achieved in this work (as shown in Fig. 9c), regardless of whether it was clean water, seawater, sandy groundwater, or dye-including effluent. Based on the efficient water transportation sub-component, accompanied by a carbon heat collector on the top, a solar vapor generation rate of 2.0 kg m^{-2} h^{-1} and energy utilization efficiency of 85.7% were realized under 1 sun illumination. The impressive water extraction speed exhibited great promise on a broad range of occasions and might be beneficial for future solar vapor generation with a reduced water contact area.

Apart from reducing the thermal loss, the scheme of water transportation could also play a positive role in enhancing vapor generation. Inspired by the super liquid transportation property of the asymmetric capillary ratchet of a bird's beak and the peristome surface of a pitcher plant, Wu *et al.*[29] designed and fabricated a reverse cone-shaped solar evaporator with asymmetric grooves and microcavity arrays on the surface. Owing to the unique surface design, water was able to move upwardly and spread perpendicularly on the device in a mere 100 ms. Consequently, a water film with inhomogeneous thickness along the sidewall was formed, with an apex liquid film thickness of ~15 μm and a bottom liquid film thickness of ~1500 μm. The much thinner liquid film on the apex had a higher tendency to vaporize than the bottom liquid layer, resulting in a water evaporation rate of ~0.84 kg m^{-2} h^{-1} even without solar flux. The position-dependent temperature distribution was another issue to assist the water evaporation. As shown in Fig. 9d, the surface temperature of the evaporator decreased with increasing elevation. Such a temperature difference could induce a thermocapillary effect to drive the water upward from the bulk water. With the special water transportation effect and efficient energy utilization on the 3D evaporator, a water evaporation rate of 2.63 kg m^{-2} h^{-1} was achieved under 1 sun illumination.

4.1.2 Reduced water contact area. Apart from manipulating the water transportation pathway, reducing the water contact area has been proved to be effective in reducing thermal loss.[108,109] To narrow down the water transportation pathway, Ni and co-workers[14] created a floating multi-layer solar evaporation device, composed of solar absorbing fabric as the photothermal layer, expanded polystyrene foam as the floating insulator, and white cellulose fabric as the water transportation pathway (as shown in Fig. 10a). The expanded polystyrene with low thermal conductivity (~0.02 W m^{-1} K^{-1}) could limit thermal conduction, whereas the hydrophilic white fabric wick with high thermal conductivity (0.58 W m^{-1} K^{-1}) could leak heat. Thus, in order to localize thermal energy in a confined area with efficient water replenishment, a 20% wicking area and 80% insulation

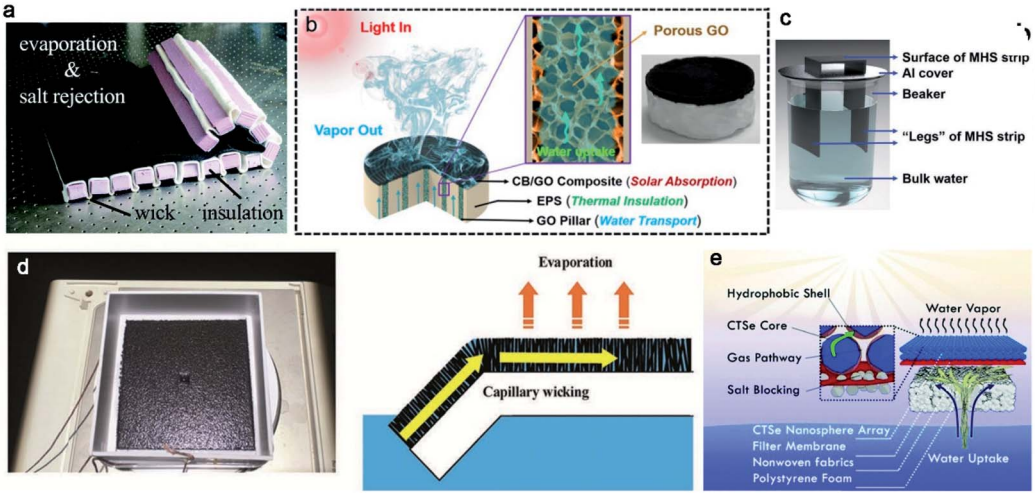

Fig. 10 Solar evaporator with reduced water contact area. (a) A floating multilayer solar evaporation device. Reproduced with permission.[14] Copyright 2018, Royal Society of Chemistry. (b) A jellyfish-like solar vapor evaporator. Reproduced with permission.[27] Copyright 2017, Elsevier. (c) A MOF-based hierarchical system. Reproduced with permission.[101] Copyright 2019, Wiley-VCH. (d) A (BNF) flocking board. Reproduced with permission.[81] Copyright 2019, Wiley-VCH. (e) A hydrophilic/hydrophobic nanoporous double-layer structure. Reproduced with permission.[41] Copyright 2018, Royal Society of Chemistry.

area were proposed and resulted in 11% energy loss by the water transportation process.

The water contact area was reduced by structural design. For example, Li and co-workers[27] designed a jellyfish-like solar vapor evaporator with a restrained water transportation pathway. As shown in Fig. 10b, due to the structural design, efficient water replenishment in the aligned GO pillars suppressed heat dissipation through water convection. As a result, an impressive energy utilization efficiency of 87.5% under 1 sun illumination was achieved. In another example, Ma and co-workers[110] prepared a MOF-based hierarchical system with two side 'legs' in the liquid to demonstrate the water evaporation process (as shown in Fig. 10c). Owing to the superior hydrophilic feature of the MOF system, water can be efficiently transported to the photothermal layer and the surface temperature cooled from 56 °C to 31 °C in 60 s, giving a final water evaporation rate of 1.50 kg m^{-2} h^{-1}. A one-dimensional water pathway was integrated in a solar evaporator by Yang *et al.*,[43] as shown in Fig. 10e. Due to the reduced contact area toward water, 86.6% of solar energy was utilized for vapor generation with a water evaporation rate of 1.657 kg m^{-2} h^{-1}. To further narrow down the water contact area, Tu *et al.*[87] fabricated a black nylon fiber (BNF) flocking board with a water-introducing hole (5 mm × 5 mm) in the middle (as shown in Fig. 10d). Owing to the strong capillary effect, a maximum radius of the wetted area of 13.2 cm was observed under 1 sun illumination. Moreover, the corresponding thermal loss driven by the water convection was even lower than that of air convection.

4.2 Anti-salt clogging

Conventionally, the salt crystals can be removed by simply cooling and washing the solar evaporator several times.[111] However, this strategy may not be appropriate for large-scale operation and runs a high risk of increasing the maintenance costs and reducing productivity in the long run. Therefore, solar vapor evaporators with self-cleaning properties are highly desirable.[14,18,29,112] In recent years, in order to address this challenge, several novel strategies have been proposed, including (1) multidirectional mass transfer; (2) Janus structure designs for brine separation; and (3) localized salt crystallization. To some extent, these methods have achieved efficient anti-salt clogging and maintained solar evaporation functions in long-term operation.

4.2.1 Multidirectional mass transfer. Ni *et al.*[14] fabricated a salt-rejecting evaporation structure with a multilayer configuration. Using the assumption of diffusion, an area ratio of 1 to 4 between the wicking area and the insulation area was chosen based on the daily mass of salt to be rejected. As shown in Fig. 11a and b, under 1 sun illumination, the evaporation structure was capable of dissolving 40 grams of additional solid salts on the photothermal surface into the brine water underneath, leading to an increase in brine concentration from 3.5 wt% to 26 wt%. Although remarkable salt rejection has been accomplished by this device, the overall solar energy utilization was ~56%, resulting from thermal convection loss and light reflective dissipation.

Kuang and co-workers[18] reported a self-regenerating solar evaporator with excellent antifouling features using a rationally designed artificial channel-array in natural wood for long-term solar vapor generation. As shown in Fig. 11c, under sunlight illumination, salt concentration gradients were formed between micro-sized natural wood channels and milli-sized drilled channels due to their individual hydraulic conductivities. Owing to the hierarchical structure, a mass transfer of salt occurred due to the concentration gradients between the two types of channels *via* the 1–2 μm pits on the sidewall, resulting

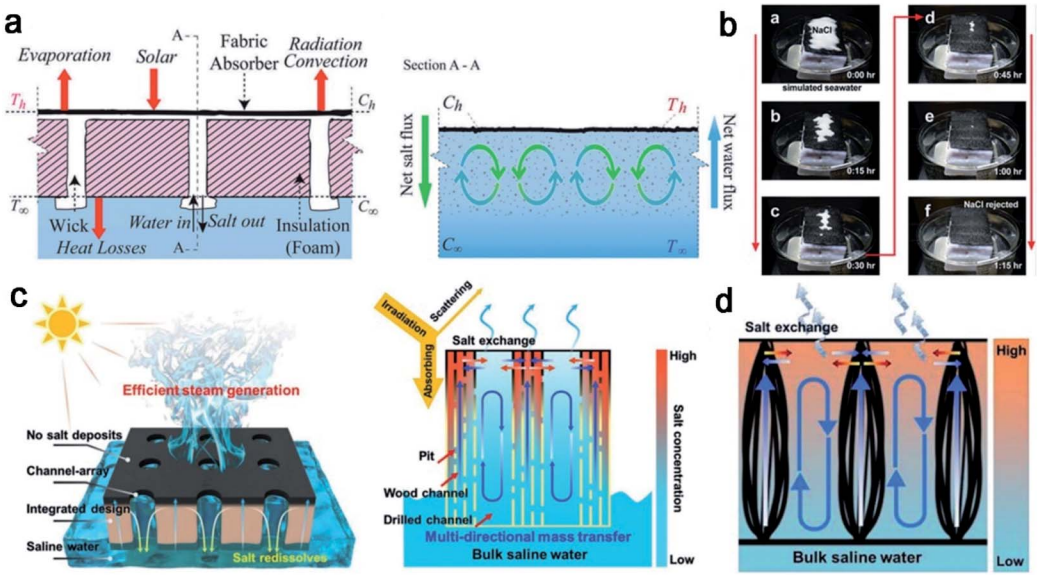

Fig. 11 Structural designs for surface salt rejection. (a and b) A schematic illustration and performance of a floating multilayer solar evaporation structure for surface rejection. Reproduced with permission.[14] Copyright 2018, Royal Society of Chemistry. A schematic illustration of multi-directional mass transfer of accumulated salts by (c) drilled carbonized wood. Reproduced with permission.[18] Copyright 2019, Wiley-VCH. (d) Artificial composite fabric. Reproduced with permission.[104] Copyright 2018, Royal Society of Chemistry.

in reduced salt accumulation in the system. In addition, the drilled channels with high hydraulic conductivities possessed a high potential to exchange with bulk water and functioned as salt-rejection pathways. Due to the smart structural designs, a solar energy efficiency of ~75% and long-term functional stability were achieved. Similar work by He *et al.*[28] applied carbonized balsa wood as the bimodal solar evaporation device. Taking advantage of the hierarchical and interconnected microstructures of balsa wood, which consisted of large vessel channels (180 to 390 μm) and narrow tracheid channels (18 to 39 μm) and micro-sized pits (~1 to 2 μm) and nanopores on the walls of the microchannels, rapid brine water replenishment and efficient salt rejection were achieved due to the capillary effect and the concentration gradient. However, although the carbonized balsa wood demonstrated efficient salt rejection properties, the solar evaporation rate of 0.8 kg m^{-2} h^{-1} and energy utilization efficiency of ~57% appeared to be insufficient under 1 sun illumination.

Wang *et al.*[113] applied the difference in hydraulic conductivities in an artificial solar evaporation system to achieve an efficient anti-salt function. With blank hollow spacer fabric as the template, chitosan as the filler and reduced graphene oxide as the surface coating, a salt-resistant solar absorber was fabricated. As shown in Fig. 11d, due to the aligned big channel array (2 mm) inside the absorber, an efficient salt–liquid exchange between the porous fiber cluster and the big channel occurred, resulting in a continuously reducing salt accumulation. Moreover, due to the porous textile fabric structure, good photothermal conversion and limited thermal conductivity of the solar absorber, an efficient energy utilization of 86% with an evaporation rate of 1.4352 kg m^{-2} h^{-1} was achieved under 1 sun illumination.

4.2.2 Janus structure designs for brine separation. To avoid salt crystallization in a solar evaporation device after water evaporation, Zhao *et al.*[38] proposed a hydrophobic MXene membrane to counter liquid infiltration. The non-wettable surface efficiently blocked the brine water underneath and let the generated vapor escape through the surface gap. Long-term stable solar vapor generation was ensured under 1 sun illumination over 200 h without any noticeable solid deposition. However, the strong hydrophobicity may also affect the water supply, and resulted in a solar evaporation rate of 1.31 kg m^{-2} h^{-1} with a solar vapor conversion efficiency of 71%. To address this drawback, Yang *et al.*[43] further modified the membrane configuration and designed a Janus hydrophilic/hydrophobic double layer for efficient long-term water desalination. The hydrophobic salt-resistant layer of well-defined nanoparticle arrays served as a photothermal layer and vapor pathway, while the hydrophilic filer membrane served as the brine water replenishment pathway. As shown in Fig. 12a, in the Janus configuration, water cannot immerse the photothermal layer; thus the process of concentrating brine only occurs beneath the hydrophobic layer. In contrast, the all-hydrophilic membrane can be immersed in brine water and precipitates solid salt crystals as the water evaporates. The salt-rejection properties of the Janus and all-hydrophilic systems were further compared by illumination with sunlight for a continuous 10 hours. A layer of salt crystals appeared on the all-hydrophilic systems while the Janus system remained clean and dry. Due to the salt-resistant feature of the Janus double layer and reduced thermal loss in this work, stable and efficient solar generation was accomplished with an evaporation rate of 1.657 kg m^{-2} h^{-1}, solar energy efficiency of 86.6%, and long-term stability over 15 days.

Almost at the same time, Xu and co-workers[114] proposed a flexible Janus absorber composed of an upper hydrophobic

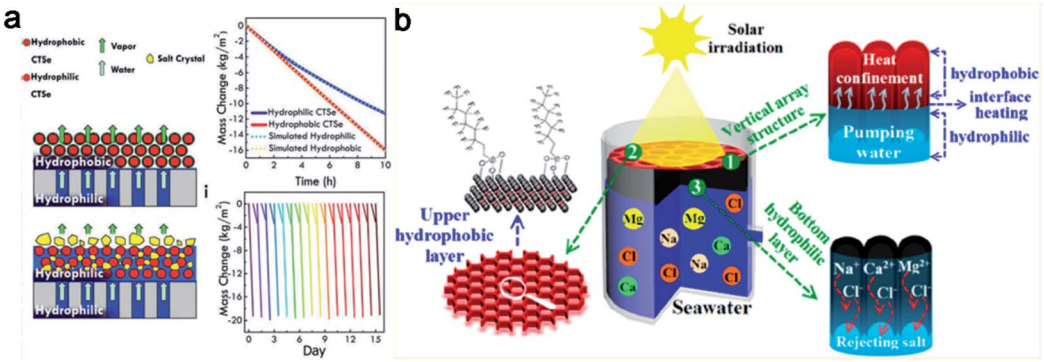

Fig. 12 (a) A schematic illustration of the Janus membrane and hydrophilic membrane for salt-rejection. Reproduced with permission.[41] Copyright 2018, Royal Society of Chemistry. (b) A schematic illustration of the Janus MXene aerogel with well-ordered vertical porous channels for highly efficient long-term solar water evaporation. Reproduced with permission.[106] Copyright 2019, American Chemical Society.

photothermal layer and a bottom hydrophilic water-supply layer for long-term solar evaporation. Under sunlight illumination, the upper layer can efficiently convert solar energy into heat for water evaporation while blocking the salt deposition underneath. Hence, the salt deposited in the hydrophilic layer can rapidly be dissolved due to the continuous water pumping. Under 1 sun illumination, an evaporation rate of 1.3 kg m^{-2} h^{-1} and solar energy efficiency of 72% were accomplished by the Janus system. In addition, the performance of solar vapor generation was sustained over 16 days, and indicated excellent salt rejection properties and strong structural durability.

Although salt-resistance was achieved using the Janus system, the relatively low energy utilization efficiency remained a major drawback due to the thermal convection loss to bulk water. Although external water pumping components have been proposed to ameliorate this issue, the structural durability problem may cause new concerns. To address these challenges, Zhang *et al.*[115] designed a vertically aligned Janus MXene aerogel with well-ordered vertical porous channels, selected channel diameters and structure thickness to perform efficient long-term solar vapor generation (as shown in Fig. 12b). Compared with irregular porous channels, the well-aligned porous channels exhibited a competitive advantage in water transportation, light absorption, and vapor escape. With an optimized channel diameter of 15 μm, a water transport rate of 0.54 g min^{-1} was achieved that laid a solid foundation for brine replenishment and salt dissolution. In addition, with a structure thickness of 10 mm, a good balance between thermal localization and vapor efficiency was achieved, resulting in a water evaporation rate of ~1.46 kg m^{-2} h^{-1} and solar energy efficiency of 87%. Furthermore, due to the intact structure of the Janus aerogel, a nearly constant water yield was maintained for 15 days.

4.2.3 Localized salt crystallization. Previous efforts have been devoted to reducing the salt concentration inside the solar evaporation system and hence preserve the vapor generation performance in long-term operation. In contrast, the localized salt crystallization method offers a new strategy for maintaining continuous vapor production while harvesting the solid salts from seawater. Xia *et al.*[17] designed and fabricated a disc-shaped solar vapor generator that achieved vapor generation and solid salt harvesting at the same time. As shown in Fig. 13a and b, the brine water can be efficiently pumped to the evaporation surface and diffused in a radial manner. Under sunlight illumination, salt crystallized at the edge location as water evaporated. Fig. 13c clearly indicates the salt mass distribution on the evaporator. Moreover, due to the edge-preferential

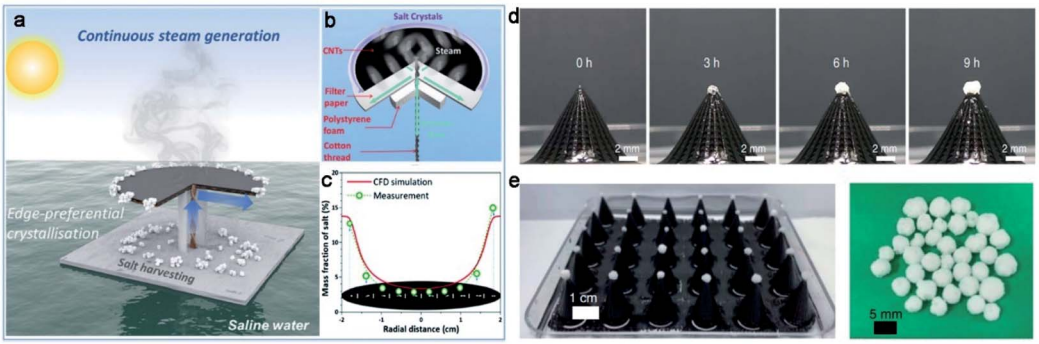

Fig. 13 Schematic illustration of (a) edge-preferential salt crystallization and (b) brine water transportation. (c) The mass fraction of salt on the evaporation disc. Reproduced with permission.[17] Copyright 2019, Royal Society of Chemistry. (d) The localized salt crystallization of reversed cone-shaped solar evaporator at different time points. (e) Solid salt collection by an array of solar evaporators. Reproduced with permission.[29] Copyright 2020, Nature Springer.

crystallization property, the solar evaporation performance remained nearly constant for over 600 h of operation.

Another localized salt crystallization strategy was proposed by Wu *et al.*,[29] who designed a reversed cone-shaped solar evaporator with a bio-mimetic surface structure. As mentioned in Section 4.1.1, the super liquid transportation properties of the solar evaporator and reversed surface temperature gradient can efficiently transport water from the bottom site to the apex, resulting in strong vapor production on the top. Consequently, salt crystallized at the apex with growing diameter as water evaporated, as shown in Fig. 12d. In addition, even though solid salt crystals capped the apex, the solar vapor generation remained nearly unchanged, due to the vapor escape channel in the salt crystals. The larger scale salt harvesting and water evaporation are shown in Fig. 13e. Taking advantage of water transportation, efficient energy management, and localized salt crystallization, a solar-driven water evaporation rate of 2.63 kg m^{-2} h^{-1} with an energy efficiency of >96% was realized by this evaporator under one sun illumination. Such a unique structural design offered new insight into long-term water evaporation and reuse of sea salt harvesting.

5. System designs for enhanced water yield

Water collection is the last but most important step in solar vapor generation, considering the ultimate goal of freshwater production. However, previous efforts in this field have mainly focused on efficient vapor generation with comprehensive energy management,[116–118] and very much less attention has been paid to the water collection process. For a typical water collection system, the generated vapor is condensed into water on the transparent tiled roof and finally drips into a reservoir through gravity.[119–121] However, a huge discrepancy has been found between the solar-driven vapor generation rate and freshwater collection rate.[23,122,123] Table 1 summarizes the vapor/water production rate of systems with condensation systems. However, the conventional condensation setup of a transparent tiled roof could only contribute to a low water/vapor ratio (defined as the ratio of the mass of distillate to the mass of input steam). The big difference in vapor and water production can be ascribed to the optical impedance by the condensed water, absorption of sunlight by the inner vapor, and increased internal humidity as water evaporated. Therefore, creating and developing innovative designs with efficient gas–liquid transition effects and water collection rate are of paramount importance to unleashing the full potential of solar-driven freshwater production.

5.1 Modification of the condensation cover

As the place where the condensate is generated, there is no doubt that the physical properties and installation parameters of the condensation surface have significant impacts on water production. In previous research studies on solar stills, scientists have extensively investigated the properties of the condensation surface, including the type of material, surface roughness, installation inclination, shape, transmittance, and wiping and vibration of the condensing surface.[21] However, in order to achieve abundant freshwater production, the decisive factor is whether the condensation surface can maintain a continuous high solar flux. A series of plastic materials, such as acrylic,[130] PET,[21] polyesters,[14] and PMMA,[131] with high solar transmittance, light weight, and low cost, have been applied in solar vapor generators. During solar water evaporation, liquid water was formed on the bottom surface of the transparent cover. As shown in Fig. 14a, the

Table 1 The water yield of solar-driven evaporation with condensation systems

Condensation scheme	Solar absorber	Light intensity (kW m^{-2})	Water evaporation rate (kg m^{-2} h^{-1})	Water production rate (kg m^{-2} h^{-1})	Water/vapor ratio (%)	Ref.
Tiled roof	Carbon sponge	Natural sunlight	1.15	0.35	30.43	100
	Graphene assembly framework	1	2.1	0.8	38	124
	PVA–rGO hydrogel	1	~2.5	~1.3	52	40
	Cu_2SnSe_3/$Cu_2ZnSnSe_4$ film	1	1.657	0.889	53.65	43
	CNT-coated conical structure	1	2.63	1.72	65.40	29
	Polypyrrole-modified maize straw	1	3.0	2.2	73.33	125
	Commercial fabric and polystyrene foam	Natural sunlight	Not mentioned	2.5 L per m^2 per day	N/A	14
	Reduced graphene oxide/cotton fabric	1/natural sunlight	1.47	~4 L per m^2 per day	N/A	126
	PPy functionalized paper	1/natural sunlight	2.99	~6.9 L per m^2 per day	N/A	15
	Defect-abundant graphene aerogel	1/natural sunlight	1.78	9.52 L per m^2 per day	N/A	127
	AIE/all-fiber aerogel	1/natural sunlight	1.43	10.9 L per m^2 per day	N/A	128
	PVA–PPy hydrogel	1/natural sunlight	3.2	18–23 L per m^2 per day	N/A	23
Vapor manipulation	PVA–Ti_2O_3 hydrogel	1	~3.6	~1.3–3	36.11–83.33	19
	Polypyrrole (PPy) Origami Rose	1	1.72–2.25	1.52–2.11	88.37–93.77	77
Latent heat recovery	Two-stage solar distiller	1	0.98	1.02	1.04	129
	Multi-stage solar distiller	1	—	3	N/A	26
	Multi-stage solar distiller	1	5.78	~4.34	75.08	13

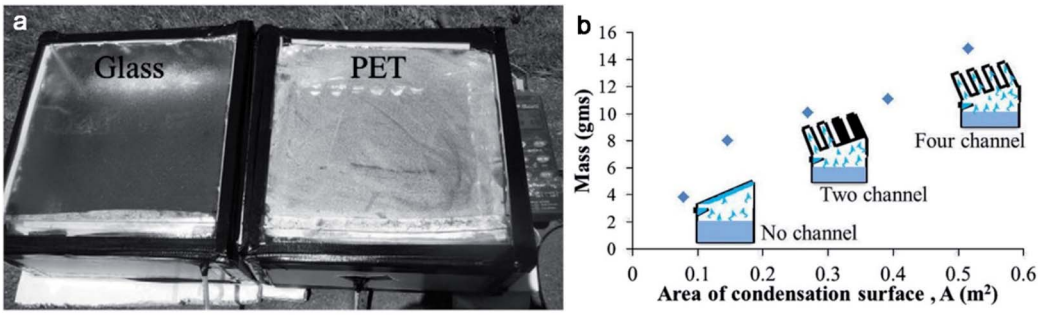

Fig. 14 (a) The transparency of glass and PET condensation covers during solar evaporation. Reproduced with permission.[21] Copyright 2013, Elsevier. (b) The effect of condensation surface on the water collection rate. Reproduced with permission.[22] Copyright 2015, Elsevier.

hydrophobic nature of PET plastic would significantly reduce the light transmittance due to surface-dangling water droplets. In contrast, for hydrophilic glass,[132] although it is heavy, brittle, and has higher production costs, the continuous excellent light transmittance may result in a nearly 30% enhanced water collection rate. Therefore, it is urgent to discover or develop an alternative material for the condensation surface with a hydrophilic nature, high transparency, light weight, and low fabrication costs.

The productivity of freshwater from a solar evaporation device is also influenced by the temperature difference between the condensation surface and the inner vapor. It has been found that with an increasing temperature discrepancy across the condensation surface, higher water production was achieved.[48] Therefore, in order to improve the productivity, various cooling methods, including external water flows,[133,134] external air flows,[135] and enlarged condensation surfaces[22] have been reported. Inside the solar water evaporation system, the circulation of air mass was increased by keeping up the temperature discrepancy between the solar absorber and the condensation cover. With a reduction in glass cover temperature in the range of 6–20 °C, an improvement in water productivity of 20% has been achieved in an outdoor experiment. However, cooling the condensation cover by a flowing water film or air requires additional energy input, which significantly undermines the sustainable and economical nature of solar evaporation. In contrast, increasing the temperature difference by enlarging the condensation area is an attractive strategy to enhance the freshwater production rate. Bhardwaj *et al.*,[22] provided a flexible and reliable way to enhance freshwater production by enlarging the condensation area. As shown in Fig. 14b, with additional channels integrated on the evaporation cover, an increased amount of vapor was recovered for condensation. To a certain extent, the additional channels can be seen as air-flow condensers, which exacerbate the temperature difference across the condensation cover and improve the water productivity. According to the authors, the production of water from the evaporation system was enhanced by over five fold by increasing the condensation area from 0.08 to 0.52 m^2.

5.2 Manipulation of vapor pressure

In a closed system, evaporation and condensation occur reversibly, following the equation H_2O (l) ↔ H_2O (g). In order to facilitate vapor production and thereby strengthen condensation, it is necessary to reduce the vapor pressure and drive the phase transition direction. It has been proved that wind can accelerate water vapor generation due to the induced surface negative pressure. Liu *et al.*[20] have studied the effect of wind-driven negative pressure on vapor generation. With a geopolymer–biomass mesoporous carbon composite as the solar absorber, the vapor production rate was examined under 1 sun illumination at different wind speeds. Water evaporation rates of 2.85, 5.90, and 7.55 kg m^{-2} h^{-1} were obtained under 1 sun illumination at wind speeds of 1, 2, 3 m s^{-1}, respectively. Such values far exceed that of the natural water evaporation rate (0.502 kg m^{-2} h^{-1}), indicating that an increase in wind speed can efficiently promote the water evaporation rate. A saturated evaporation rate was obtained at high wind speed and under a strong solar flux due to the limitation in water transportation underneath. Although an efficient strategy to enhance the water evaporation rate was offered by the authors, a freshwater collection experiment was not mentioned.

Zhang *et al.*[136] designed and fabricated a simple all-in-one solar distillation device for practical seawater desalination. As shown in Fig. 15a, the device is composed of two chambers: an evaporation chamber and a condensing chamber. Under sunlight exposure, the generated vapor was guided to the condensing chamber by a solar-powered electrical fan. Due to the enhanced circulation of the air mass and air-cooled evaporation surface, a water production rate of 0.15 kg m^{-2} h^{-1} was obtained, which was 15 times higher than that from natural evaporation. Although the water production rate in this work was not promising due to the absence of a thermal management scheme, the demonstrated concept provided a direction for vapor manipulation in the early stages of this field.

A more sophisticated solar evaporation system was reported by Guo *et al.*[19] They fabricated a light-absorbing sponge-like hydrogel composed of Ti_2O_3 nanoparticles and a PVA chain for highly efficient water evaporation. Due to the energy nano-confinement and water activation effects, a record high vapor generation rate of up to ~3.6 kg m^{-2} h^{-1} was obtained under 1 sun irradiation in an open system. However, the intrinsic water production rate of this system was ~1.3 kg m^{-2} h^{-1}, due to the rapidly saturated relative humidity, which significantly inhibited the vapor production from the hydrogel system. To

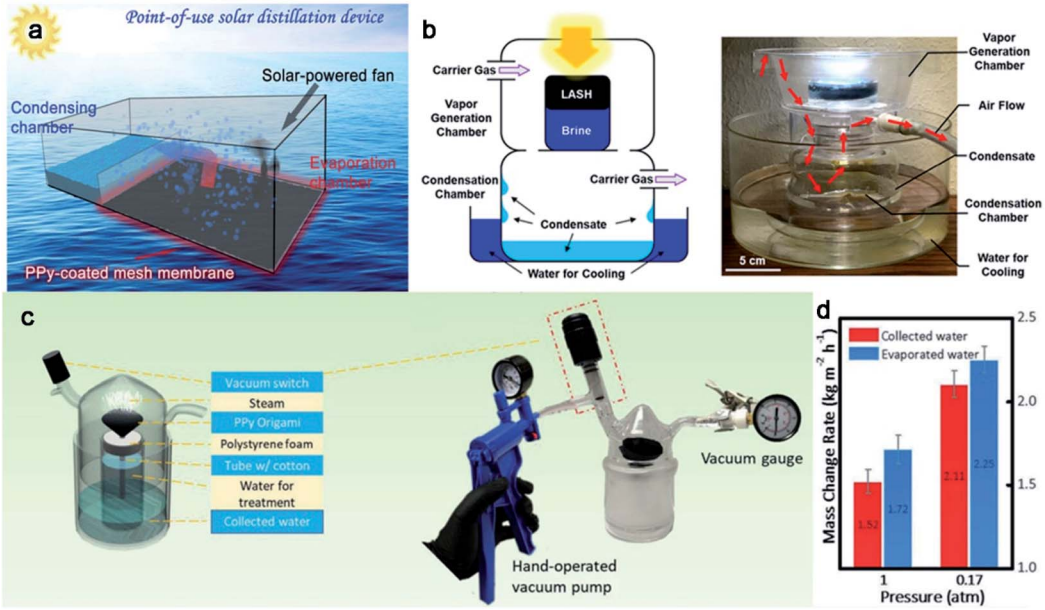

Fig. 15 Schematic illustration of water collection by vapor manipulation by (a) a simple and all-in-one solar distillation device. Reproduced with permission.[127] Copyright 2015, Wiley-VCH. (b) A light-absorbing sponge-like hydrogel with air flow. Reproduced with permission.[19] Copyright 2019, American Chemical Society. (c) A low-pressure solar steaming-collection unisystem. (d) The performance of vapor and water production under different inner pressures. Reproduced with permission.[77] Copyright 2019, Wiley-VCH.

overcome this obstacle, airflow was introduced to transport the generated vapor from the evaporation chamber to the condensation chamber to reduce the vapor pressure (as shown in Fig. 15b). With the aid of a pump, as the speed of the air flow increased from 0, to 10, and to 40 ml min^{-1}, the water delivery rate increased from ~1.3, to 2.2, and ~3 kg m^{-2} h^{-1}, respectively. The enhanced water production rate was attributed to the reduced humidity induced by the negative pressure. Similar work was reported by Li *et al.*,[77] who utilized a low-pressure solar steaming-collection unisystem to reduce the vapor pressure inside the evaporation system (Fig. 15c). As shown in Fig. 15d, under a reduced pressure of 0.17 atm, the water evaporation rate and water collection rate were hugely promoted from 1.72 to 2.25 kg m^{-2} h^{-1} and from 1.52 to 2.11 kg m^{-2} h^{-1}, respectively, compared to ambient pressure.

Although the water production rate was significantly enhanced by reducing the vapor pressure, the energy consumption in this system was not mentioned, and thus the capability of the device for freshwater production cannot be fully evaluated. As claimed by Li *et al.*,[77] such a design may be appropriate for portable application in an emergency. For large-scale solar water evaporation, novel designs with efficient vapor manipulation are urgently needed for sustainable and economically efficient freshwater production.

5.3 Latent heat recovery

When condensing water vapor with a transparent cover, a large amount of latent heat is discharged into the ambient. Such a process occurs regardless of the sunlight absorption capability of solar absorbers and the comprehensive thermal insulation schemes used for water evaporation. Further recovery and utilization of the latent heat could greatly enhance the freshwater productivity.[137] However, it seems impossible to harvest the dissipated latent heat by the typical configuration of a solar-driven evaporation system. A photothermal membrane distillation (PMD) system, with a reversed configuration of feed water and generated vapor, exhibited great potential to recover latent heat. PMD is a thermally activated separation process in which the separation is driven by a phase transition. A hydrophobic membrane/layer is applied to inhibit water transportation but allows only vapour to pass through it. Such a process is driven by a partial vapour pressure difference across the hydrophobic layer along with solar-to-thermal generation. In the typical configuration of a PMD system, the feed side of the liquid water source is located on the hydrophobic membrane, while the vapor is condensed on the opposite side after penetrating the membrane. Compared to a solar-driven evaporation scheme, PMD may also have natural advantages in salt rejection and anti-fouling.

Hence, Xue *et al.*[129] first proposed a compact solar–thermal membrane distillation system with the features of localized solar–thermal heating, effective cooling, and latent heat recovery. The evaporation system was composed of a commercial solar absorber (Bluetec, Germen) for heat generation, a PVA sponge for seawater transportation, hydrophobic membranes for antifouling, and two metal collectors for vapor condensation. As shown in Fig. 16a, with solar light as the only energy input, water evaporation and condensation occur sequentially in Collector 1 and Collector 2, which indicates reutilization of the latent heat. The temperatures of the internal vapor and water collector in the two stages are shown in Fig. 16b, which provided good evidence for energy propagation and recycling.

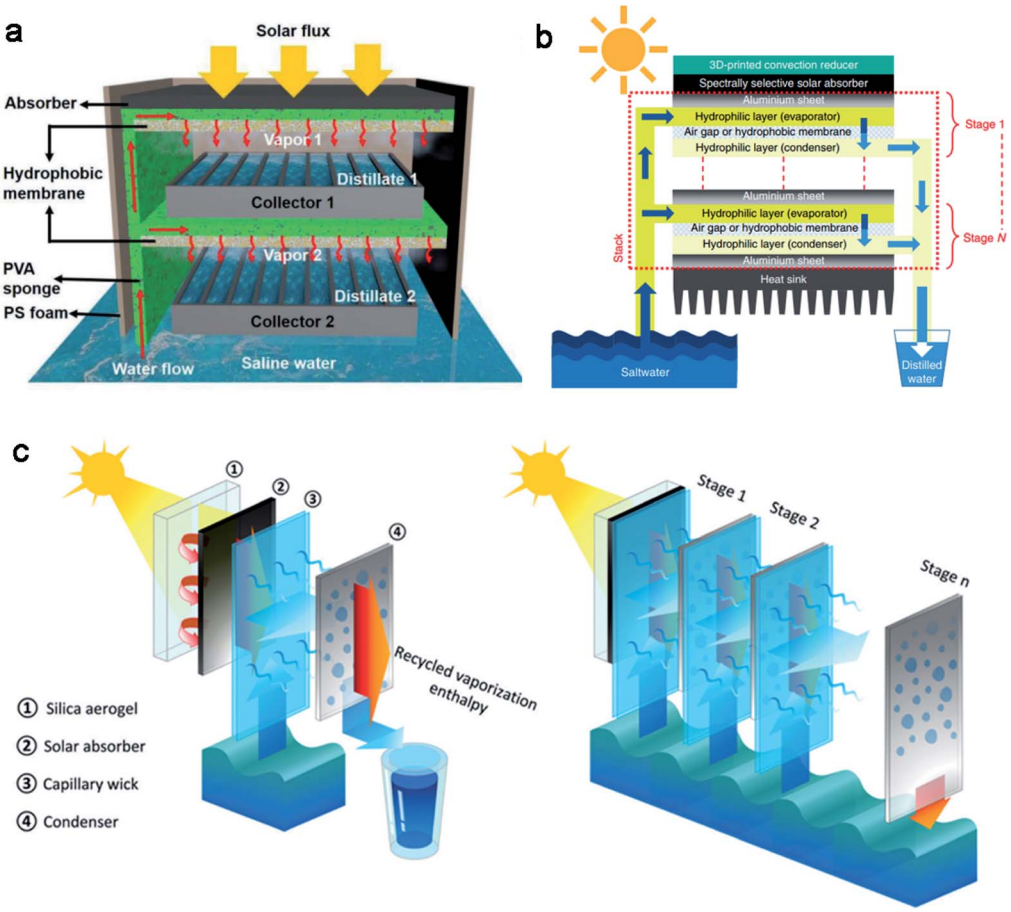

Fig. 16 Water yield enhancement by latent heat recovery. (a) A schematic illustration of a two-stage latent heat recovery device. Reproduced with permission.[123] Copyright 2018, Wiley-VCH. (b) A schematic illustration of a multiple-stage latent heat recovery device. Reproduced with permission.[26] Copyright 2018, Nature Springer. (c) A schematic illustration of another multiple-stage latent heat recovery system and the detailed device configuration. Reproduced with permission.[13] Copyright 2020, Royal Society of Chemistry.

Owing to the novel energy management strategy, a water collection rate of 1.02 kg m^{-2} h^{-1} with a solar efficiency of 72% was obtained under 1 sun illumination, whereas a vapor generation rate of 0.98% m^{-2} h^{-1} was achieved in the open system.

A similar but more elaborate system was proposed by Chiavazzo *et al.*[26] They designed and fabricated a passive multistage and low-cost solar distiller to recover the phase transition latent heat for enhancing the freshwater yield. Each unit stage for distillation was composed of two hydrophilic layers and an intermediate hydrophobic microporous layer. As the heat-induced vapor was generated from the first hydrophilic layer and condensed in the second hydrophilic layer, the latent heat was recovered as the secondary thermal source to activate another around of vaporization in devices with a multilayer configuration. Hence, the dependence of water productivity on the number of stages was confirmed. Specifically, the 3- and 10-stage configurations exhibited threefold and six-fold higher water productivity than the single-stage configuration in laboratory experiments. Owing to the latent heat recovery strategy, an impressive water collection rate of 3 L m^{-2} h^{-1} was accomplished by the 10-stage configuration device under 1 sun illumination.

Xu and co-workers[13] further elaborated the designs of the multistage architecture by adjusting the structural parameters with simulation outcomes. As shown in Fig. 16c, the multistage architecture is composed of a solar absorbing stage and numbers of evaporation/air/condensation stages. The width of the device a, the air gap distance b between the evaporation and condensation membranes, and the total number of stages n were proved to be of great significance in water and vapor transportation and thermal energy dissipation. In order to maximize practicability, a trade-off between theoretical performance and practical limitations was made, which resulted in a configuration of $a = 10$ cm, $b = 2.5$ mm and $n = 10$. Eventually, the designed multistage solar distiller exhibited a record-high freshwater production rate of 5.78 L m^{-2} h^{-1} with a solar-to-vapor conversion efficiency of 385% under 1 sun illumination, which evidenced efficient latent heat recycling and reutilization. However, the single-stage configuration only gave a water production rate of 1.21 L m^{-2} h^{-1} with a solar-to-vapor conversion efficiency of 81%, under 1 sun illumination. In general, the latent heat recovery strategy leads to totally different system configurations to the interfacial solar evaporation models, however, with remarkably high energy

reutilization. The significance of the multistage device is that it is more than a novel way to improve freshwater productivity, but more importantly, it sheds new light on the solar water evaporation field and provides a steady step up for future commercialization.

6. Recent progress in applications

With the ever-deepening research into solar-driven vapor generation, various novel solar-absorbing materials, comprehensive structural designs, and sophisticated energy management schemes have been proposed to bring the solar evaporation devices to maturity and promote system performance, which have laid a solid foundation for future applications. Despite its nature of energy sustainability and environmental friendliness, solar vapor generation still suffers unignorable limitations and drawbacks in its current stage, such as low freshwater productivity, large footprint requirements, and weather-dependent performance. Nevertheless, in recent years, scientists have put forward many profound and interesting ideas based on mass and energy transfer and transformation within solar evaporation, including seawater desalination,[138–140] sewage purification,[84,141,142] and even electricity generation.[112,143] To some extent, these ideas play a guiding role leading to future solar-evaporation-based applications and enriching their development possibilities. In this section, we review cutting-edge solar evaporation applications and discuss the underlying mechanism and application potentials.

6.1 Seawater desalination

Considering the ultimate goal of alleviating water scarcity, solar-driven water treatment methods have exhibited great potential in freshwater production for their unlimited energy and water resources,[144] minor environmental impact, and long-term and automatic operation. Compared to current membrane-filtering technologies, solar-driven evaporation is less susceptible to the quantity and quality of the water source and is thus capable of producing clean water from diverse situations, including seawater,[145] household sewage, and industrial wastewater[146] in a cost-efficient way. However, conventional solar-driven water production solutions suffer from low energy utilization efficiency[147] and high capital construction costs,[83,148] which have significantly impeded their development and practical applications.

In the past few years, due to drastic changes in the mindset of energy utilization, from volumetric bulk heating,[149,150] to interfacial heating,[151] and to isolation localized heating,[29] the energy efficiency of solar-still-type systems has increased dramatically and provided a steady step up for future practical applications.[10] Currently, numerous solar-evaporation devices with enhanced solar evaporation efficiency, salt rejection property, miniaturized structures, and affordable costs have been reported. For example, Zhou *et al.*[40] demonstrated a hydrogel-based solar evaporator with a high energy efficiency of ~95% under one sun for solar desalination (Fig. 17a). The solar evaporation hydrogel was prepared by *in situ* gelation of polyvinyl alcohol (PVA) with a loading of reduced graphene oxide (rGO). Upon sunlight irradiation, the internal PVA hydrogel network can efficiently transport water and confine the thermal energy generated by the embedded rGO, enabling a steady water production rate of ~1.3 kg m^{-2} h^{-1} under one sun illumination in a closed system. The desalination effect of the solar evaporation device was further examined by testing a real seawater sample (from the Gulf of Mexico) and three artificial seawater samples with representative salinities from the Baltic Sea (0.8 wt%), the World Ocean (3.5 wt%), and the

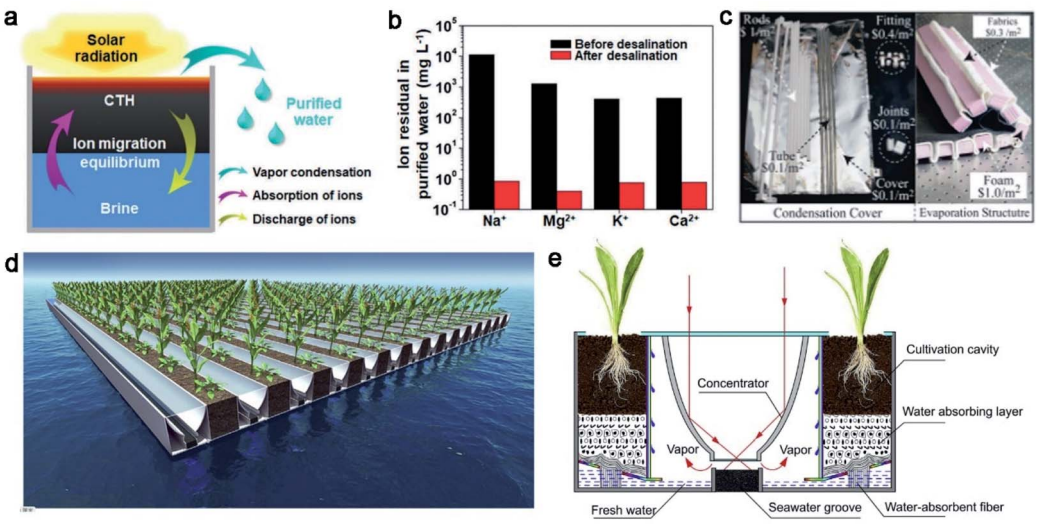

Fig. 17 A schematic illustration of (a) hydrogel-based seawater purification. (b) The ion concentration before and after desalination. Reproduced with permission.[38] Copyright 2018, Royal Society of Chemistry. (c) An illustration of the fabrication costs of a floating solar still. Reproduced with permission.[14] Copyright 2018, Royal Society of Chemistry. A schematic illustration of (d) marine agriculture accomplished by a floating transparent device. (e) The freshwater production process. Reproduced with permission.[138] Copyright 2018, Elsevier.

Dead Sea (10 wt%). As shown in Fig. 17b, the concentration of primary ions was measured by inductively coupled plasma (ICP) spectrometry and the results indicate that the salinity of the condensed water is nearly four orders of magnitude lower than the initial solution, and two orders of magnitude lower than the drinking water standards defined by the World Health Organization (WHO, 1‰) and the US Environmental Protection Agency (EPA, 0.5‰). In addition, the functional stabilities of the device were verified under 1 sun illumination for over 96 continuous hours without noticeable change, indicating its excellent durability for long-term practical applications.

The unit cost of water production is another important issue in solar-driven seawater desalination. Ni *et al.*[14] reported a floating multilayer solar evaporation structure for practical solar desalination. The flexible assembly materials made this system easily deployed for desalination in off-grid and remote areas. In an outdoor experiment, a floating solar still on the ocean (Pleasure Bay, Boston, USA) could produce freshwater at 2.5 L per m^2 per day with solar-to-water efficiency of 22%, which was enough to satisfy daily individual drinking needs. As shown in Fig. 17c, the cost of materials of the entire solar evaporation system was ~$3 per m^2, which was 10–100 times lower than current solar still systems. Moreover, with an estimated life cycle of 2 years, the unit cost of water production was nearly $1.5 per m^3, 10 times lower than that of conventional solar still devices. Although current plant-based membrane-filtering water desalination had a lower unit cost ($0.5 per m^3), high capital funding inhibited its operation in remote water-stressed and disaster-stricken communities.

Beyond purifying seawater for drinking, solar water evaporation could also shed new light on the development of marine agriculture. Wang and co-workers[152] designed and fabricated a floating transparent device with multiple horizontal grooves and a special interior structure. As shown in Fig. 17d and e, the parabolic-shaped surface can efficiently concentrate solar light to thermalize the seawater absorbing material for water evaporation and the side chamber can condense the hot vapor to generate freshwater for crop irrigation. Under 1000 W m^{-2} irradiation, the water production rate of the proposed floating device was calculated as 195.1 g m^{-2} h^{-1} with an energy efficiency of 16.5%. The performance of the water production rate was relatively low, possibly due to the absence of a thermal energy management scheme. However, the concept proposed by Zhang *et al.* may enrich the possibility of applications based on solar-driven desalination.

6.2 Sewage purification

Although the ocean possesses the most abundant water resource for freshwater generation, in daily life, household sewage and industrial wastewater have a more intimate relationship with human activities. Various contaminants, including heavy metal ions,[146] organic compounds,[153] oil and grease,[110] and bacteria[154] in wastewater exhibit severe toxicity not only to living species but also to the environment. In this age, how to recycle and revitalize a clean water resource from contaminated water is of wide concern. Currently, solar water evaporation may provide an effective solution to deal with this issue by separating and condensing the water vapor under sunlight illumination.

Based on the promising solar–thermal response of graphene, Zhang *et al.*[124] fabricated a housing self-supply water system with a highly vertically ordered pillar array framework (HOPGF). With well-defined structures, a solar vapor generation rate of 2.10 kg m^{-2} h^{-1} with an energy efficiency of 95% was achieved

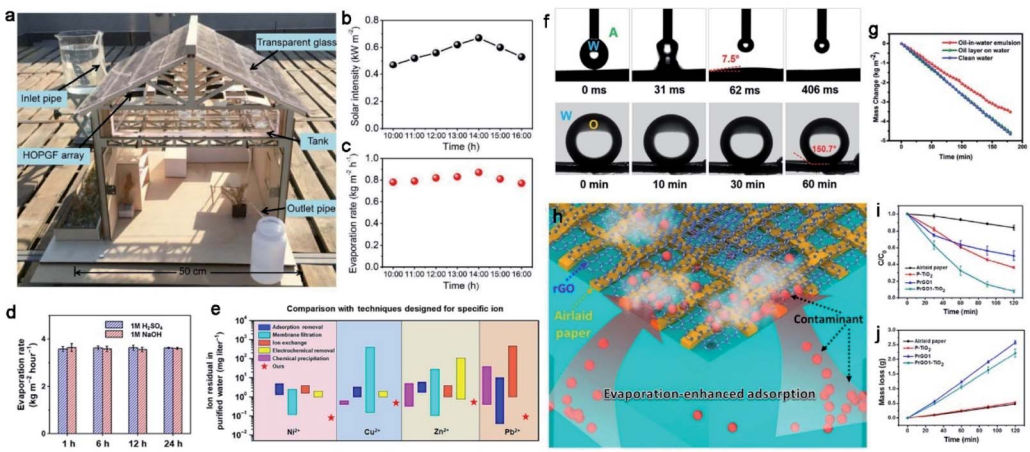

Fig. 18 (a) The prototype model of a housing self-supply water system. (b) The intensity of solar flux at different time points and (c) the corresponding water evaporation rate. Reproduced with permission.[141] Copyright 2018, Royal Society of Chemistry. (d) The performance of water evaporation in strong acid and alkali. (e) A comparison of the rejection of heavy metals by a hydrogel system with other commercial approaches. Reproduced with permission.[142] Copyright 2019, American Association for the Advancement of Science. (f) Water contact angle analysis indicated that a MOF-based evaporator exhibited a strong hydrophilic property. (g) The water evaporation rate of the MOF-based evaporator in oil-containing wastewater. Reproduced with permission.[101] Copyright 2019, Wiley-VCH. (h) A schematic illustration of solar–thermal based decontamination with evaporation-enhanced physical adsorption and photocatalytic degradation. (i) The performance of the photocatalytic degradation of RhB with solar evaporators of different configurations. (j) The water evaporation rate of solar evaporators with different configurations. Reproduced with permission.[139] Copyright 2016, American Chemical Society.

under 1 sun illumination in an open system. The HOPGF was firstly examined for purifying seawater and raw pharmaceutical wastewater (acid, alkaline, and neutral solutions) and the collected purified water was measured with neutral pH and low conductivity. Based on the capabilities of HOPGF, the authors designed and proposed a proof-of-concept housing self-supply water system to realize the cyclic utilization of household sewage. As shown in Fig. 18a, HOPGF arrays are fixed under a transparent rooftop to acquire sufficient solar energy for water evaporation. The household wastewater was drawn to the solar absorber by cotton threads through capillary effects and the hot vapor was condensed on the glass rooftop. According to Fig. 18b and c, even under a moderate solar flux of 0.6 sun and ambient temperature of 15 °C, an average water production rate of 0.8 kg m^{-2} h^{-1} was achieved by this system. Moreover, according to the authors, for a building with a roof area of 100 m^2, 480 kg of clean water can be collected in a day, which is sufficient to satisfy the daily needs of seven people. Hence, the proposed housing self-supply water system exhibited great promise to realize the cyclic utilization of household sewage for future domestic applications.

To acquire clean water from industrial sewage, Zhou *et al.*[89] introduced a highly hydratable light-absorbing hydrogel to achieve efficient water evaporation. According to the authors, enhancing the hydratability of the hydrogel can change the water state and partially activate the water for evaporation, resulting in a water evaporation rate of ~3.2 kg m^{-2} h^{-1} with an energy efficiency of ~92% under 1 sun irradiation. Based on such an impressive performance of solar evaporation, the hydrogel device also exhibited excellent wastewater purification results. As shown in Fig. 18d, a steady water evaporation rate was obtained in strong acid (1 M H_2SO_4) and alkali (1 M NaOH) solutions, and the purified water appeared to have neutral pH. In addition, nearly four orders of magnitude lower heavy metal ions were obtained by the hydrogel device, which was comparable with current commercial purification methods (Fig. 18e). Oils and/or other organic compounds are always contained in real wastewater and may lead to severe fouling problem of solar evaporation devices. Ma *et al.*[110] reported a MOF-based solar–thermal water evaporator to counter the organic contaminants in the wastewater. Owing to the strong hydrophilic properties of the hierarchical MOF structure, the oil contaminant can be efficiently repelled. The Janus features are indicated in Fig. 18f. As shown in Fig. 18g, the water evaporation performance was nearly constant in water with an oil layer and slightly reduced in an oil-in-water emulsion, compared to clean water.

The combination of a photothermal and a porous structure could provide new insights into sewage treatment. For example, Lou *et al.*[153] reported paper-based composites composed of reduced graphene oxide (rGO) sheets, porous air-laid paper, and titanium dioxide (TiO_2) nanoparticles for multifunctional solar-driven clean water generation. As shown in Fig. 18h, with the porous structure of the paper substrate and enhanced photothermal response of rGO, contaminants can be efficiently removed through physical absorption with the aid of evaporation-based upward diffusion. Furthermore, taking advantage of photothermal effects and localized pollutant accumulation, a highly efficient photodegradation of rhodamine B (RhB) in water was accomplished by the embedded TiO_2 nanoparticles. As shown in Fig. 18i and j, over 95% of the RhB in the solution was removed by the composite paper under solar illumination for 2 h and the integration of photocatalytic components exhibited only a 10% lower water evaporation rate, which indicated a feasible combination in this work. Moreover, after 4 h of treatment by the composited paper, both the condensed water and the purified water appeared colourless and shared the same absorbance spectra, which indicated excellent decontaminant properties.

6.3 The evaporation-assisted electricity generation

Innovative designs that tackle two global challenges, freshwater and energy scarcity, under sunlight irradiation are of great value to human society. In recent years, the emergence of interfacial solar evaporation has offered new insights into electricity generation. Due to its heat confinement configuration, ameliorated surface temperature,[85] relatively facile preparation processes,[155] and versatile deployable features,[156] solar water evaporation can be applied on a broad range of occasions with high energy utilization efficiency. Recent advances have demonstrated evaporation-assisted electricity generation,[157] which is based on the physical changes in the evaporation system under sunlight illumination, including temperature differences across the solar evaporator, salinity accumulation beneath the solar absorber,[158] frictional contact induced by downward water flow,[156,159] and horizontal water flow[160] in the evaporation surface, *etc.* It should be mentioned that evaporation-assisted electricity generation is not comparable to photovoltaic (PV) technology; however, as an extra bonus, evaporation-assisted electricity generation can partially ameliorate energy scarcity in a humble way. In this section, conceptual ideas for the dual generation of freshwater and electricity are reviewed.

Previously, numerous research studies focused on enhancing the vapor generation and water production rate under solar illumination have been reported. However, the internal enthalpy of steam was usually lost to the ambient as vapor condensed to water, resulting in a huge energy loss. To acquire and reutilize this part of the energy, Li *et al.*[161] introduced a novel concept to generate clean water and electricity simultaneously by storing and recycling vapor enthalpy derived from solar-driven steam generation. As shown in Fig. 19a–c, under light illumination, hot vapor was extensively generated and condensed to produce clean water, while the energy in the vapor was reserved in the thermal storage chamber. The huge temperature discrepancy between the chamber and the ambient environment was utilized to generate electricity by using thermoelectric modules. Under the optimal situation, the solar energy utilization efficiency for vapor generation reached 72.2% and electricity generation reached 1.23%. Such a performance was sufficient for the operation of an electric fan and 28 light-emitting diodes. Unlike generating electricity by hot vapor, the thermalized solar absorber can induce thermoelectricity directly.[162] As shown in Fig. 19d and e, a sponge-type solar

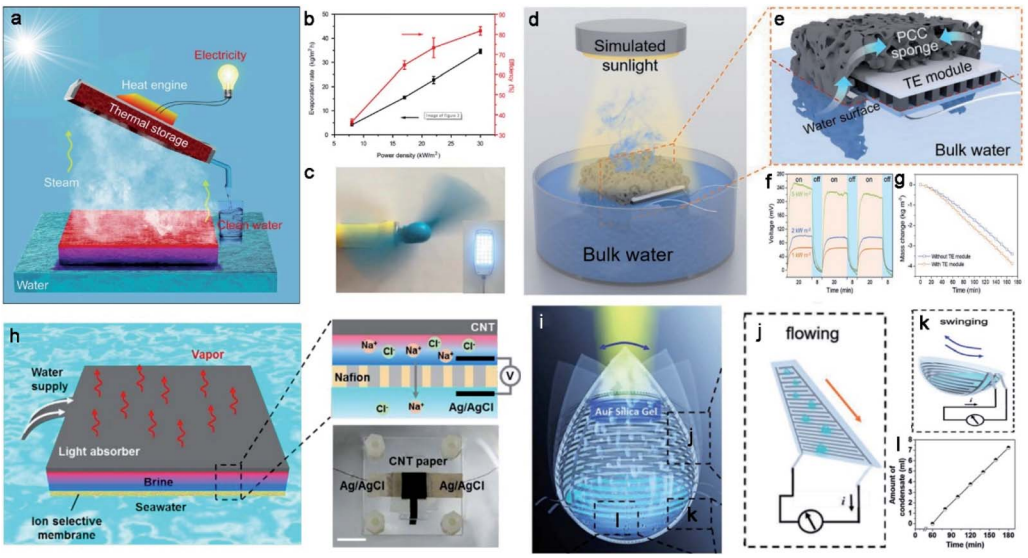

Fig. 19 A schematic illustration of solar evaporation accompanied by electricity generation. (a, d and e) Illustrate thermal electricity based on hot vapor and a thermalized solar absorber. The performance of the dual-functional devices is demonstrated in (b, c, f and g). Reproduced with permission.[149] Copyright 2018, Elsevier. Reproduced with permission.[150] Copyright 2019, Wiley-VCH. (h) The electricity induced by salinity gradient across a Nafion membrane. Reproduced with permission.[146] Copyright 2017, Elsevier. (i and j) A schematic illustration of harvesting triboelectric energy *via* the downward flow of condensate droplets. (k) The wind energy can be harvested due to the swinging of the device. (l) The water collection amount was recorded over time. Reproduced with permission.[144] Copyright 2018, Wiley-VCH.

evaporator is placed directly on the TE module, which generates electricity based on the Seebeck effect triggered by the temperature discrepancy between the illuminated sponge and bulk water. As shown in Fig. 19f and g, with an optimal external resistance of 2 Ω, a maximum output power density of 0.4 W m^{-2} was achieved under 1 sun irradiation. Notably, the coupling of solar evaporation and thermo-electric technologies was realized without trade-offs, with an evaporation efficiency of 87.4% under 1 sun illumination.

Apart from thermal generation, the salinity difference induced by water evaporation has also been applied for the generation of electricity. Yang and co-workers[158] proved that the salinity difference between evaporation-accumulated liquid and seawater can be utilized for electricity generation. The authors prepared a hybrid system composed of a carbon nanotube (CNT) modified filter paper and an additional ion-selective membrane (a Nafion membrane) to generate water vapor and an ion gradient at the same time. As shown in Fig. 19h, as water is continuously being evaporated, high-concentration salt water is confined in a limited space between the CNT paper and the Nafion membrane for electricity generation. The water evaporation and electricity generation increased with enhanced solar power and a maximum water evaporation rate of 1.1 kg m^{-2} h^{-1} and electricity power of ~1 W m^{-2} were achieved under one sun illumination.

Taking advantage of the downward flow of condensate droplets, Gao *et al.*[156] fabricated a proof-of-concept prototype to collect the condensation water and to harness triboelectric energy at the same time. As shown in Fig. 19i–l, the prototype consists of inclined walls and a round bottom vessel (lined with PTFE energy harnessing triboelectric nanogenerator (TENG) devices), and water evaporator hydrogel. Under sunlight illumination, the generated vapor was condensed on the tiled walls as tiny water droplets and grew bigger and flowed down to the collection vessel with gravity. The flow of the water droplets generated electricity due to the electrification of the water and the PTFE, which resulted from the negatively charged PTFE and the positively charged water droplets. Moreover, wind energy, which can affect the flow conditions of condensate droplets and electrification of the prototype system, can also be harvested. According to the authors, the maximum peak power obtained by this system was 0.63 μW with an evaporation efficiency of ~85% under one sun illumination.

Electricity generated from the evaporation-driven water flow was recognized as a newly developed form of green energy in recent years.[163] Xiao and his co-workers[160] proposed a novel concept to realize an efficient combination of solar evaporation and horizontal water-flow-induced power generation by an asymmetrically functionalized Janus material. The dual-functional solar evaporation device was composed of a bilayer of carbon nanotubes (CNTs)/cellulose paper partially covered by hydrophobic polydimethylsiloxane (PDMS) on the bottom. Due to the confined water flow in the membrane device, the directional proton flow enabled electricity generation. It was proved that the ion concentration, solar light intensities, and load resistance all significantly affected the power generation. In the optimal situation, a maximum output power of 2.1 μW and 1.15 kg m^{-2} h^{-1} were accomplished by the Janus device under one sun illumination.

Solar-driven evaporation is a process which involves multiple physical changes, such as thermal generation, salinity gradient enhancement, condensation of vapor, and water transportation.

Taking advantage of those processes may help to produce extra electrical energy. It has to be accepted that the productivity of evaporation-assisted electricity is far lower than that of PV technology (around 1 or 2 orders lower). However, the electricity generation is accompanied by solar-driven evaporation as a by-product but not as the main product. The innovative designs of dual-functional solar-driven evaporation provides a feasible pathway to ameliorate water and energy scarcity at the same time. However, the previously mentioned research works in this section have mainly been accomplished in an indoor environment, which may not have enough reliability to sustain the same performance in practical applications.

7. Conclusion and outlook

7.1 Conclusion and discussion

A solar evaporation strategy has become one of the technologies with greatest potential to tackle water scarcity over the past few years. Previous reports focused on thermal-driven water evaporation with photothermal conversion and utilization as the main directions.[31] Thus, great strides have been made in the design and fabrication of solar absorbers and remarkable vapor production rates have been achieved in an open system.[20,23] However, solar evaporation is a pluralistic process, involving energy absorption and manipulation, water transportation, and water collection. Freshwater yield, as the ultimate goal, is a more direct metric for the performance evaluation of solar distillers.

Recent advances in solar evaporation have revealed the significance of system designs of functional modules on overall performance enhancement. Energy absorption is considered to be the foundation for water evaporation. In order to enlarge the total energy input of a solar-driven evaporation device, modification of surface topography, energy concentration scheme, and achieving environmental energy strategies have been summarized in this review article. These proposed strategies have all demonstrated positive effects in enhancing the water evaporation rate. Specifically, by modifying the surface structures, a solar absorber is capable of minimizing light reflection and compensating for the variation in solar angles, which strengthen solar absorption. Such a design is especially beneficial for day-long solar-related applications. We envision the huge potential of this strategy, since performance enhancement can be achieved by other devices by simply copying the designed surface pattern. Motivated by the optical concentration method, a thermal concentration scheme was proposed to achieve high-temperature (100 °C) vapor under natural sunlight. Previously, efforts were devoted to increasing the interface temperature as much as possible in order to accelerate the water evaporation process. The emergence of a thermal concentration scheme shed new light on thermal-to-vapor conversion. However, the large footprint requirement and intensified heat loss of this scheme, significantly hinder its development in solar evaporation under current system configurations. Nevertheless, we still believe the thermal concentration scheme has huge unexplored potential to exploit, which will require further development and motivation from research communities. Recovering environmental energy is an efficient method to boost the water evaporation rate beyond the theoretical upper limit. In a typical design for cold vapor generation, elaborate surface structures and intensified vapor escape are required to realize the low surface temperature (below room temperature) of the device. In this case, an energy flow from a warmer environment to the evaporation device occurs, which enlarges the energy input for vapor generation. Although the water evaporation rate can be enhanced significantly by recovering environmental energy, it is a great challenge to condense the cold vapor to boost the water production rate. Hence, further development is necessary to come up with a solution to address the condensation problem.

The water transportation module plays a significant role in building the connection between solar absorbers and water bodies. However, the water flows across the solar absorber take most of the thermal energy, which is considered to be the major heat-draining pathway. In order to achieve efficient solar evaporation, it is necessary to maintain a good balance between thermal generation and water transportation. Currently, such a goal can be accomplished either by designing the water supply pathway or by reducing the water contact area. For example, Zhao *et al.*[23] prepared a PVA gel-based evaporation device with a hierarchical internal structure for water replenishment, which contributes a 0.90 μm s^{-1} bottom water transport rate and 0.89 μm s^{-1} surface water loss rate. Li *et al.*[27] fabricated a composite evaporation device with jellyfish-like water wicking channels, resulting in a reduced water contact area and heat conduction loss. Previous attempts had already proven the capability and feasibility of system designs of the water pathway in improving the energy utilization and water evaporation rate. Hence, it is of great importance to adopt these concepts in practice. Salt crystallization in a solar-driven evaporation system can significantly undermine the performance of water evaporation by increasing the optical reflectance and impeding water and vapor transportation. To address this challenge, multidirectional mass transfer, Janus structures, and localized salt crystallization methods have been proposed in the last two years. Although multidirectional mass transfer and Janus structures have proven to be effective in salt-rejection for a long continuous working period, the adopted system design may compromise the water evaporation rate. In short, the multidirectional mass transfer method relies on the difference between salt gradient and hydraulic conductivity to reject salt back into bulk water. Such a strategy requires sufficient water exchange between the evaporation system and bulk water, resulting in enhanced heat conduction loss. To reject salt accumulation by a Janus evaporation system, the thickness of the hydrophobic top layer is critical, for which a thin layer may not be efficient to counter salt solution infiltration and a thick layer may not be efficient in preventing the escape of water vapor. Moreover, the membrane configuration of a Janus structure shows a relatively high thermal loss. Hence, further improvements are necessary to establish these two strategies before applying them in real-world applications. In contrast, the localized salt crystallization method, which does not inhibit the salting-out behaviour but induces crystallization in desired places, is a promising approach to perform water evaporation without compromise.

Moreover, this approach can not only recover the freshwater, but can also collect salt crystals as a recyclable source. Therefore, localized salt crystallization exhibits greater value and potential for commercialization.

Water collection as the final step in the solar evaporation process has gained increasing interest recently. In a conventional vapor condensation design, the gas–liquid transition is performed on a transparent tiled cover and water is collected by downflow with gravity. However, a huge discrepancy between the water evaporation rate and the water production rate has been found, due to the optical impedance of the condensation cover, sunlight absorption by inner vapor, and inner saturated humidity. In order to overcome these obstacles, researchers have provided three strategies to combat the phenomena from different angles. The first strategy to enhance the freshwater yield is to change the structural features of the condensation cover. For example, enhancing the hydrophilicity of the inner cover surface can promote the formation of a water film and reduce the water droplets, resulting in enhanced light transmittance. Enlarging the area of the condensation cover can increase the temperature discrepancy across the cover and hence promote the gas–liquid transition. Currently, glass has proven to be the most effective materials for a condensation cover. The structural features mentioned above are feasible for realization on glass with current technology. However, the fabrication costs and lifetime maintenance are other concerns to be considered. Manipulation of the vapor has proven to be highly effective in enhancing the freshwater production rate. The introduction of negative pressure can not only accelerate the vapor collection rate, but can also promote water evaporation. However, a fact that cannot be ignored is that the negative pressure requires additional energy input. Such energy consumption makes the entire solar evaporation process complex and difficult to handle, especially in large-scale solar distillation. Therefore, further studies are required to balance the energy input and freshwater output and to consider the whole process in a comprehensive manner. Very recently, a latent heat recovery strategy was reported to enhance the water collection rate by recycling and reutilizing the released latent heat. In a conventional system setup, the latent heat energy is dissipated to the environment once the gas–liquid phase transition has occurred on the condensation cover. By reversing the vapor escape direction, the latent heat can be recycled with a multistage condensation configuration. Remarkably, a record high water evaporation rate of 5.78 kg m^{-2} h^{-1} and a water collection rate of ~4.34 kg m^{-2} h^{-1} were realized using a 10-stage solar-driven evaporation system.[13] In general, latent heat recovery sheds new lights on freshwater production with enhanced energy utilization. Considering the promising performances in solar evaporation, it will be beneficial to adopt this strategy in real-world applications.

7.2 Challenges and perspectives

Regardless of the fast and extensive developments in the solar evaporation field, there are still multiple challenges that require further study to bring solar evaporation into practice in real-world applications. With the trend of approaching commercialization, it is necessary to optimize and balance the issues of freshwater efficiency, environmental impacts, functional stability, scalability and fabrication costs of solar-driven evaporation systems.

Recent breakthroughs in the system design of solar absorbers with a comprehensive thermal management scheme have efficiently boosted the water evaporation rate; however, obtaining freshwater from the gas–liquid transition is still in its infancy. In the previous sections, we have mentioned that cold vapor driven by environmental energy can efficiently upregulate the overall water evaporation rate, with a value far higher than the theoretical limit. However, owing to the intrinsic low temperature of a cold vapor, it is difficult to condense it on the condensation cover due to the reversed temperature discrepancy (the cold vapor has a lower temperature than the ambient). In contrast, hot vapor condensation can be easily enhanced by modification of the condensation cover, the introduction of negative pressure, and the recycling of latent heat. However, the fabrication cost of the condensation surface, the extra energy input of negative pressure, and the scale-up problems in a multistage latent heat recovery system may bring about new concerns to be overcome.

Previous efforts of solar distillation were accomplished under laboratory conditions with brine or even pure water as the water source. However, when considering practical applications, it is inevitable that one must face diverse types of water sources, such as seawater, river water, ground water, and industrial and household sewage, which may contain a large amount of uncertain contaminants, such as metal ions, oil and grease, organic compounds, and bacteria. Resistance to these contaminants is essential for maintaining the functional and structural integrities of solar evaporators. For example, fouling by organic compounds may affect the physical properties of a solar absorber, resulting in a reduced water evaporation rate. The high operating temperature may accelerate the corrosion of the solar evaporation device in high-salinity water. Salt clogging in the solar evaporators may increase the surface light reflection and limit the water transportation pathways, thus affecting the long-term operational productivity. Although great efforts have been made to overcome fouling by diverse contaminants *via* material engineering and structural designs and have achieved effective results, in most cases, there is a trade-off with the performance of solar distillation. Hence, creating a novel solution to counteract various water sources over a wide range of conditions for long-term high-performance solar evaporation poses a challenging task.

When faced with commercialization, the scalability and cost of a solar evaporator are two important factors affecting the competitiveness of this technology. However, most reported cases did not provide a systematic analysis of cost or mention the scale-up potential for real-world implementation. Previous reports paid much more attention to performance enhancement in water evaporation than to cost analysis. The expenses of raw materials, fabrication and design costs of solar evaporators, and lifetime maintenance need to be specified and compared to existing purification and desalination technologies to promote

acceptance by potential customers. Moreover, previous and current studies focused mainly on the unit performance of solar evaporators, and the potential for large-scale solar evaporation was not evaluated in a quantitative way. Hence, a greater focus on this aspect is necessary to direct the solar evaporation technology into commercialization. Future research studies for developing new solar evaporation systems should give more consideration to the cost-effectiveness issue and a systematic analysis method for evaluating the large-scale potential is highly desirable.

Given the nearly unlimited solar energy source and diverse water sources, solar evaporation technology with a facile preparation process, low capital investment, zero carbon footprint, and automatic operation is considered to be the most promising technology to tackle water scarcity in this age. Although there are still multiple challenges to be addressed with the current technology, we foresee great developments in solar evaporation in the coming decade. In order to help research communities to catch the development trend in this field, we have summarized recent advances in solar evaporation with clear functional partitioning. In addition, we hope this review can help readers quickly grasp an overview of current solar evaporation technologies and stimulate the sparking of thoughts on the exploration of advanced technologies to tackle water scarcity with unlimited energy and water sources.

Conflicts of interest

There are no conflicts to declare.

Acknowledgements

This research is supported by the National Natural Science Foundation of China (No. U1801254, 51925805), the Project of Department of Education of Guangdong Province (No. 2018KZDXM060) and the Natural Science foundation of Guangdong Province (2019A1515012163), a grant from the Research Grants Council of the Hong Kong Special Administrative Region, China (PolyU 15200518) and The Hong Kong Polytechnic University (G-UAHK).

References

1 J. Schewe, J. Heinke, D. Gerten, I. Haddeland, N. W. Arnell, D. B. Clark, R. Dankers, S. Eisner, B. M. Fekete, F. J. Colón-González, S. N. Gosling, H. Kim, X. Liu, Y. Masaki, F. T. Portmann, Y. Satoh, T. Stacke, Q. Tang, Y. Wada, D. Wisser, T. Albrecht, K. Frieler, F. Piontek, L. Warszawski and P. Kabat, *Proc. Natl. Acad. Sci. U. S. A.*, 2014, **111**, 3245.
2 J. H. Reif and W. Alhalabi, *Renewable Sustainable Energy Rev.*, 2015, **48**, 152–165.
3 M. M. Mekonnen and A. Y. Hoekstra, *Sci. Adv.*, 2016, **2**, e1500323.
4 M. Elimelech and W. A. Phillip, *Science*, 2011, **333**, 712.
5 D. Zarzo and D. Prats, *Desalination*, 2018, **427**, 1–9.
6 J. Kim, K. Park, D. R. Yang and S. Hong, *Appl. Energy*, 2019, **254**, 113652.
7 S. Lattemann and T. Höpner, *Desalination*, 2008, **220**, 1–15.
8 P. Tao, G. Ni, C. Song, W. Shang, J. Wu, J. Zhu, G. Chen and T. Deng, *Nat. Energy*, 2018, **3**, 1031–1041.
9 O. Neumann, A. S. Urban, J. Day, S. Lal, P. Nordlander and N. J. Halas, *ACS Nano*, 2013, **7**, 42–49.
10 J. Zhou, Y. Gu, P. Liu, P. Wang, L. Miao, J. Liu, A. Wei, X. Mu, J. Li and J. Zhu, *Adv. Funct. Mater.*, 2019, **29**, 1903255.
11 P. Mu, Z. Zhang, W. Bai, J. He, H. Sun, Z. Zhu, W. Liang and A. Li, *Adv. Energy Mater.*, 2019, **9**, 1802158.
12 G. Chen, N. Zhang, N. Li, L. Yu and X. Xu, *Adv. Mater. Interfaces*, 2020, **7**, 1901715.
13 Z. Xu, L. Zhang, L. Zhao, B. Li, B. Bhatia, C. Wang, K. L. Wilke, Y. Song, O. Labban, J. H. Lienhard, R. Wang and E. N. Wang, *Energy Environ. Sci.*, 2020, **13**, 830–839.
14 G. Ni, S. H. Zandavi, S. M. Javid, S. V. Boriskina, T. A. Cooper and G. Chen, *Energy Environ. Sci.*, 2018, **11**, 1510–1519.
15 F. Ni, P. Xiao, C. Zhang, Y. Liang, J. Gu, L. Zhang and T. Chen, *ACS Appl. Mater. Interfaces*, 2019, **11**, 15498–15506.
16 Y. Shi, R. Li, Y. Jin, S. Zhuo, L. Shi, J. Chang, S. Hong, K.-C. Ng and P. Wang, *Joule*, 2018, **2**, 1171–1186.
17 Y. Xia, Q. Hou, H. Jubaer, Y. Li, Y. Kang, S. Yuan, H. Liu, M. W. Woo, L. Zhang, L. Gao, H. Wang and X. Zhang, *Energy Environ. Sci.*, 2019, **12**, 1840–1847.
18 Y. Kuang, C. Chen, S. He, E. M. Hitz, Y. Wang, W. Gan, R. Mi and L. Hu, *Adv. Mater.*, 2019, **31**, 1900498.
19 Y. Guo, X. Zhou, F. Zhao, J. Bae, B. Rosenberger and G. Yu, *ACS Nano*, 2019, **13**, 7913–7919.
20 F. Liu, B. Zhao, W. Wu, H. Yang, Y. Ning, Y. Lai and R. Bradley, *Adv. Funct. Mater.*, 2018, **28**, 1803266.
21 R. Bhardwaj, M. V. ten Kortenaar and R. F. Mudde, *Desalination*, 2013, **326**, 37–45.
22 R. Bhardwaj, M. V. ten Kortenaar and R. F. Mudde, *Appl. Energy*, 2015, **154**, 480–490.
23 F. Zhao, X. Zhou, Y. Shi, X. Qian, M. Alexander, X. Zhao, S. Mendez, R. Yang, L. Qu and G. Yu, *Nat. Nanotechnol.*, 2018, **13**, 489–495.
24 G. Ni, G. Li, S. V. Boriskina, H. Li, W. Yang, T. Zhang and G. Chen, *Nat. Energy*, 2016, **1**, 16126.
25 Y. Guo, F. Zhao, X. Zhou, Z. Chen and G. Yu, *Nano Lett.*, 2019, **19**, 2530–2536.
26 E. Chiavazzo, M. Morciano, F. Viglino, M. Fasano and P. Asinari, *Nat. Sustainability*, 2018, **1**, 763–772.
27 Y. Li, T. Gao, Z. Yang, C. Chen, Y. Kuang, J. Song, C. Jia, E. M. Hitz, B. Yang and L. Hu, *Nano Energy*, 2017, **41**, 201–209.
28 S. He, C. Chen, Y. Kuang, R. Mi, Y. Liu, Y. Pei, W. Kong, W. Gan, H. Xie, E. Hitz, C. Jia, X. Chen, A. Gong, J. Liao, J. Li, Z. J. Ren, B. Yang, S. Das and L. Hu, *Energy Environ. Sci.*, 2019, **12**, 1558–1567.
29 L. Wu, Z. Dong, Z. Cai, T. Ganapathy, N. X. Fang, C. Li, C. Yu, Y. Zhang and Y. Song, *Nat. Commun.*, 2020, **11**, 521.
30 L. Zhu, M. Gao, C. K. N. Peh and G. W. Ho, *Mater. Horiz.*, 2018, **5**, 323–343.
31 M. Gao, L. Zhu, C. K. Peh and G. W. Ho, *Energy Environ. Sci.*, 2019, **12**, 841–864.

32 V.-D. Dao and H.-S. Choi, *Global Challenges*, 2018, **2**, 1700094.
33 C. Zhang, H.-Q. Liang, Z.-K. Xu and Z. Wang, *Adv. Sci.*, 2019, **6**, 1900883.
34 H. Liu, Z. Huang, K. Liu, X. Hu and J. Zhou, *Adv. Energy Mater.*, 2019, **9**, 1900310.
35 Y. Lin, H. Xu, X. Shan, Y. Di, A. Zhao, Y. Hu and Z. Gan, *J. Mater. Chem. A*, 2019, **7**, 19203–19227.
36 S. Cao, Q. Jiang, X. Wu, D. Ghim, H. Gholami Derami, P.-I. Chou, Y.-S. Jun and S. Singamaneni, *J. Mater. Chem. A*, 2019, **7**, 24092–24123.
37 ASTM G173-03(2012), *Standard tables for reference solar spectral irradiances: direct normal and hemispherical on 37° tilted surface*, ASTM International, West Conshohocken, PA, 2012.
38 J. Zhao, Y. Yang, C. Yang, Y. Tian, Y. Han, J. Liu, X. Yin and W. Que, *J. Mater. Chem. A*, 2018, **6**, 16196–16204.
39 X. Yang, Y. Yang, L. Fu, M. Zou, Z. Li, A. Cao and Q. Yuan, *Adv. Funct. Mater.*, 2018, **28**, 1704505.
40 X. Zhou, F. Zhao, Y. Guo, Y. Zhang and G. Yu, *Energy Environ. Sci.*, 2018, **11**, 1985–1992.
41 K.-K. Liu, Q. Jiang, S. Tadepalli, R. Raliya, P. Biswas, R. R. Naik and S. Singamaneni, *ACS Appl. Mater. Interfaces*, 2017, **9**, 7675–7681.
42 F. P. Incropera, A. S. Lavine, T. L. Bergman and D. P. DeWitt, *Fundamentals of heat and mass transfer*, Wiley, 2007.
43 Y. Yang, H. Zhao, Z. Yin, J. Zhao, X. Yin, N. Li, D. Yin, Y. Li, B. Lei, Y. Du and W. Que, *Mater. Horiz.*, 2018, **5**, 1143–1150.
44 G. Ni, G. Li, S. V. Boriskina, H. Li, W. Yang, T. Zhang and G. Chen, *Nat. Energy*, 2016, **1**, 16126.
45 C. Finnerty, L. Zhang, D. L. Sedlak, K. L. Nelson and B. Mi, *Environ. Sci. Technol.*, 2017, **51**, 11701–11709.
46 P. Zhang, J. Li, L. Lv, Y. Zhao and L. Qu, *ACS Nano*, 2017, **11**, 5087–5093.
47 K. M. S. Eldalil, *Desalination*, 2010, **251**, 3–11.
48 Z. M. Omara, A. S. Abdullah, A. E. Kabeel and F. A. Essa, *Renewable Sustainable Energy Rev.*, 2017, **78**, 176–193.
49 V. Dimri, B. Sarkar, U. Singh and G. N. Tiwari, *Desalination*, 2008, **227**, 178–189.
50 M. Gao, P. K. N. Connor and G. W. Ho, *Energy Environ. Sci.*, 2016, **9**, 3151–3160.
51 D. P. Storer, J. L. Phelps, X. Wu, G. Owens, N. I. Khan and H. Xu, *ACS Appl. Mater. Interfaces*, 2020, **12**, 15279–15287.
52 K. Bae, G. Kang, S. K. Cho, W. Park, K. Kim and W. J. Padilla, *Nat. Commun.*, 2015, **6**, 10103.
53 Z. Wang, Y. Liu, P. Tao, Q. Shen, N. Yi, F. Zhang, Q. Liu, C. Song, D. Zhang, W. Shang and T. Deng, *Small*, 2014, **10**, 3234–3239.
54 Z. Huang, S. Li, X. Cui, Y. Wan, Y. Xiao, S. Tian, H. Wang, X. Li, Q. Zhao and C.-S. Lee, *J. Mater. Chem. A*, 2020, **8**, 10742–10746.
55 L. Zhou, Y. Tan, D. Ji, B. Zhu, P. Zhang, J. Xu, Q. Gan, Z. Yu and J. Zhu, *Sci. Adv.*, 2016, **2**, e1501227.
56 J. Li, X. Wang, Z. Lin, N. Xu, X. Li, J. Liang, W. Zhao, R. Lin, B. Zhu, G. Liu, L. Zhou, S. Zhu and J. Zhu, *Joule*, 2020, **4**, 928–937.
57 B. Zhang, C. Song, C. Liu, J. Min, J. Azadmanjiri, Y. Ni, R. Niu, J. Gong, Q. Zhao and T. Tang, *J. Mater. Chem. A*, 2019, **7**, 22912–22923.
58 C. Song, L. Hao, B. Zhang, Z. Dong, Q. Tang, J. Min, Q. Zhao, R. Niu, J. Gong and T. Tang, *Sci. China Mater.*, 2020, **63**, 779–793.
59 N. Liu, L. Hao, B. Zhang, R. Niu, J. Gong and T. Tang, *Sustainable Energy Fuels*, 2020, **4**, 5522–5532.
60 Q. Hou, C. Xue, N. Li, H. Wang, Q. Chang, H. Liu, J. Yang and S. Hu, *Carbon*, 2019, **149**, 556–563.
61 A. Celzard, A. Pasc, S. Schaefer, K. Mandel, T. Ballweg, S. Li, G. Medjahdi, V. Nicolas and V. Fierro, *Carbon*, 2019, **146**, 232–247.
62 M. Zhu, Y. Li, F. Chen, X. Zhu, J. Dai, Y. Li, Z. Yang, X. Yan, J. Song, Y. Wang, E. Hitz, W. Luo, M. Lu, B. Yang and L. Hu, *Adv. Energy Mater.*, 2018, **8**, 1701028.
63 I. Ihsanullah, *Nano-Micro Lett.*, 2020, **12**, 72.
64 X. Zhao, X.-J. Zha, J.-H. Pu, L. Bai, R.-Y. Bao, Z.-Y. Liu, M.-B. Yang and W. Yang, *J. Mater. Chem. A*, 2019, **7**, 10446–10455.
65 L. Su, Y. Hu, Z. Ma, L. Miao, J. Zhou, Y. Ning, Z. Chang, B. Wu, M. Cao, R. Xia and J. Qian, *Sol. Energy Mater. Sol. Cells*, 2020, **210**, 110484.
66 H. Zhang, Y. Wang, Y. Liu, M. Zhao, C. Liu, Y. Wang, M. K. Albolkany, N. Wu, M. Wang, L. Yang and B. Liu, *ChemSusChem*, 2020, **13**, 2945–2951.
67 J. Wang, Y. Li, L. Deng, N. Wei, Y. Weng, S. Dong, D. Qi, J. Qiu, X. Chen and T. Wu, *Adv. Mater.*, 2017, **29**, 1603730.
68 T. Li, Q. Fang, H. Lin and F. Liu, *J. Mater. Chem. A*, 2019, **7**, 17505–17515.
69 Y. Li, T. Gao, Z. Yang, C. Chen, W. Luo, J. Song, E. Hitz, C. Jia, Y. Zhou, B. Liu, B. Yang and L. Hu, *Adv. Mater.*, 2017, **29**, 1700981.
70 X. Zhao and C. Liu, *Sol. Energy*, 2020, **195**, 304–309.
71 F. Zhao, Y. Guo, X. Zhou, W. Shi and G. Yu, *Nat. Rev. Mater.*, 2020, **5**, 388–401.
72 Q. Zhu, K. Ye, W. Zhu, W. Xu, C. Zou, L. Song, E. Sharman, L. Wang, S. Jin, G. Zhang, Y. Luo and J. Jiang, *J. Phys. Chem. Lett.*, 2020, **11**, 2502–2509.
73 M. Chen, Y. Wu, W. Song, Y. Mo, X. Lin, Q. He and B. Guo, *Nanoscale*, 2018, **10**, 6186–6193.
74 S. Gao, X. Dong, J. Huang, J. Dong, F. D. Maggio, S. Wang, F. Guo, T. Zhu, Z. Chen and Y. Lai, *Global Challenges*, 2019, **3**, 1800117.
75 Y. Xu, J. Ma, D. Liu, H. Xu, F. Cui and W. Wang, *Chem. Eng. J.*, 2019, **356**, 869–876.
76 Y. Wang, C. Wang, X. Song, M. Huang, S. K. Megarajan, S. F. Shaukat and H. Jiang, *J. Mater. Chem. A*, 2018, **6**, 9874–9881.
77 W. Li, Z. Li, K. Bertelsmann and D. E. Fan, *Adv. Mater.*, 2019, **31**, 1900720.
78 S. Hong, Y. Shi, R. Li, C. Zhang, Y. Jin and P. Wang, *ACS Appl. Mater. Interfaces*, 2018, **10**, 28517–28524.
79 P. Sun, W. Zhang, I. Zada, Y. Zhang, J. Gu, Q. Liu, H. Su, D. Pantelić, B. Jelenković and D. Zhang, *ACS Appl. Mater. Interfaces*, 2020, **12**, 2171–2179.

80 X. Li, R. Lin, G. Ni, N. Xu, X. Hu, B. Zhu, G. Lv, J. Li, S. Zhu and J. Zhu, *Natl. Sci. Rev.*, 2017, **5**, 70–77.
81 Y. Bian, Y. Shen, K. Tang, Q. Du, L. Hao, D. Liu, J. Hao, D. Zhou, X. Wang, H. Zhang, P. Li, Y. Sang, X. Yuan, L. Zhao, J. Ye, B. Liu, H. Lu, Y. Yang, R. Zhang, Y. Zheng, X. Xiong and S. Gu, *Global Challenges*, 2019, **3**, 1900040.
82 X. Qian, Y. Zhao, Y. Alsaid, X. Wang, M. Hua, T. Galy, H. Gopalakrishna, Y. Yang, J. Cui, N. Liu, M. Marszewski, L. Pilon, H. Jiang and X. He, *Nat. Nanotechnol.*, 2019, **14**, 1048–1055.
83 L. A. Weinstein, J. Loomis, B. Bhatia, D. M. Bierman, E. N. Wang and G. Chen, *Chem. Rev.*, 2015, **115**, 12797–12838.
84 Q. Yang, C. Xu, F. Wang, Z. Ling, Z. Zhang and X. Fang, *ACS Appl. Energy Mater.*, 2019, **2**, 7223–7232.
85 H. Song, Y. Liu, Z. Liu, M. H. Singer, C. Li, A. R. Cheney, D. Ji, L. Zhou, N. Zhang, X. Zeng, Z. Bei, Z. Yu, S. Jiang and Q. Gan, *Adv. Sci.*, 2018, **5**, 1800222.
86 X. Li, J. Li, J. Lu, N. Xu, C. Chen, X. Min, B. Zhu, H. Li, L. Zhou, S. Zhu, T. Zhang and J. Zhu, *Joule*, 2018, **2**, 1331–1338.
87 C. Tu, W. Cai, X. Chen, X. Ouyang, H. Zhang and Z. Zhang, *Small*, 2019, **15**, 1902070.
88 X. Zhou, Y. Guo, F. Zhao and G. Yu, *Acc. Chem. Res.*, 2019, **52**, 3244–3253.
89 X. Zhou, F. Zhao, Y. Guo, B. Rosenberger and G. Yu, *Sci. Adv.*, 2019, **5**, eaaw5484.
90 J. Tang, T. Zheng, Z. Song, Y. Shao, N. Li, K. Jia, Y. Tian, Q. Song, H. Liu and G. Xue, *ACS Appl. Mater. Interfaces*, 2020, **12**, 18504–18511.
91 N. Xu, J. Li, Y. Wang, C. Fang, X. Li, Y. Wang, L. Zhou, B. Zhu, Z. Wu, S. Zhu and J. Zhu, *Sci. Adv.*, 2019, **5**, eaaw7013.
92 J. Liu, Q. Liu, D. Ma, Y. Yuan, J. Yao, W. Zhang, H. Su, Y. Su, J. Gu and D. Zhang, *J. Mater. Chem. A*, 2019, **7**, 9034–9039.
93 Z. Li, J. Zhang, S. Zang, C. Yang, Y. Liu, F. Jing, H. Jing, J. Hu, C. Wang and Y. Zhou, *Nano Energy*, 2020, **73**, 104834.
94 X. Wang, Q. Gan, R. Chen, H. Peng, T. Zhang and M. Ye, *ACS Sustainable Chem. Eng.*, 2020, **8**(21), 7753–7761.
95 Y. Shi, C. Zhang, R. Li, S. Zhuo, Y. Jin, L. Shi, S. Hong, J. Chang, C. Ong and P. Wang, *Environ. Sci. Technol.*, 2018, **52**, 11822–11830.
96 X. Meng, J. Yang, S. Ramakrishna, Y. Sun and Y. Dai, *ACS Sustainable Chem. Eng.*, 2020, **8**, 4955–4965.
97 C. Liu, C. Cai and X. Zhao, *ACS Sustainable Chem. Eng.*, 2020, **8**, 1548–1554.
98 Y. Yang, Y. Sui, Z. Cai and B. Xu, *Global Challenges*, 2019, **3**, 1900004.
99 Q. Chen, Z. Pei, Y. Xu, Z. Li, Y. Yang, Y. Wei and Y. Ji, *Chem. Sci.*, 2018, **9**, 623–628.
100 L. Zhu, M. Gao, C. K. N. Peh, X. Wang and G. W. Ho, *Adv. Energy Mater.*, 2018, **8**, 1702149.
101 C. Xiao, W. Liang, L. Chen, J. He, F. Liu, H. Sun, Z. Zhu and A. Li, *ACS Appl. Energy Mater.*, 2019, **2**, 8862–8870.
102 L. Yang, G. Chen, N. Zhang, Y. Xu and X. Xu, *ACS Sustainable Chem. Eng.*, 2019, **7**, 19311–19320.
103 Y. Yang, X. Yang, L. Fu, M. Zou, A. Cao, Y. Du, Q. Yuan and C.-H. Yan, *ACS Energy Lett.*, 2018, **3**, 1165–1171.
104 N. Xu, X. Hu, W. Xu, X. Li, L. Zhou, S. Zhu and J. Zhu, *Adv. Mater.*, 2017, **29**, 1606762.
105 X. Hu, W. Xu, L. Zhou, Y. Tan, Y. Wang, S. Zhu and J. Zhu, *Adv. Mater.*, 2017, **29**, 1604031.
106 C. Chen, Y. Li, J. Song, Z. Yang, Y. Kuang, E. Hitz, C. Jia, A. Gong, F. Jiang, J. Y. Zhu, B. Yang, J. Xie and L. Hu, *Adv. Mater.*, 2017, **29**, 1701756.
107 W. Xu, Y. Xing, J. Liu, H. Wu, Y. Cui, D. Li, D. Guo, C. Li, A. Liu and H. Bai, *ACS Nano*, 2019, **13**, 7930–7938.
108 W. Huang, P. Su, Y. Cao, C. Li, D. Chen, X. Tian, Y. Su, B. Qiao, J. Tu and X. Wang, *Nano Energy*, 2020, **69**, 104465.
109 Z. Yu, S. Cheng, C. Li, L. Li and J. Yang, *ACS Appl. Mater. Interfaces*, 2019, **11**, 32038–32045.
110 Q. Ma, P. Yin, M. Zhao, Z. Luo, Y. Huang, Q. He, Y. Yu, Z. Liu, Z. Hu, B. Chen and H. Zhang, *Adv. Mater.*, 2019, **31**, 1808249.
111 H. Ren, M. Tang, B. Guan, K. Wang, J. Yang, F. Wang, M. Wang, J. Shan, Z. Chen, D. Wei, H. Peng and Z. Liu, *Adv. Mater.*, 2017, **29**, 1702590.
112 Y. Zhang, T. Xiong, D. K. Nandakumar and S. C. Tan, *Adv. Sci.*, 2020, **7**, 1903478.
113 F. Wang, D. Wei, Y. Li, T. Chen, P. Mu, H. Sun, Z. Zhu, W. Liang and A. Li, *J. Mater. Chem. A*, 2019, **7**, 18311–18317.
114 W. Xu, X. Hu, S. Zhuang, Y. Wang, X. Li, L. Zhou, S. Zhu and J. Zhu, *Adv. Energy Mater.*, 2018, **8**, 1702884.
115 Q. Zhang, G. Yi, Z. Fu, H. Yu, S. Chen and X. Quan, *ACS Nano*, 2019, **13**, 13196–13207.
116 C.-S. Hu, H.-J. Li, J.-Y. Wang, A. Haleem, X.-C. Li, M. Siddiq and W.-D. He, *ACS Appl. Energy Mater.*, 2019, **2**, 7554–7563.
117 Y. Pang, J. Zhang, R. Ma, Z. Qu, E. Lee and T. Luo, *ACS Energy Lett.*, 2020, **5**, 437–456.
118 W. Zhang, G. Zhang, Q. Ji, H. Liu, R. Liu and J. Qu, *ACS Appl. Mater. Interfaces*, 2019, **11**, 9974–9983.
119 D. Hao, Y. Yang, B. Xu and Z. Cai, *ACS Sustainable Chem. Eng.*, 2018, **6**, 10789–10797.
120 S.-L. Loo, L. Vásquez, U. C. Paul, L. Campagnolo, A. Athanassiou and D. Fragouli, *ACS Appl. Mater. Interfaces*, 2020, **12**, 10307–10316.
121 Q. Fang, T. Li, Z. Chen, H. Lin, P. Wang and F. Liu, *ACS Appl. Mater. Interfaces*, 2019, **11**, 10672–10679.
122 L. Zhao, C. Du, C. Zhou, S. Sun, Y. Jia, J. Yuan, G. Song, X. Zhou, Q. Zhao and S. Yang, *ACS Sustainable Chem. Eng.*, 2020, **8**, 4362–4370.
123 L. Noureen, Z. Xie, Y. Gao, M. Li, M. Hussain, K. Wang, L. Zhang and J. Zhu, *ACS Appl. Mater. Interfaces*, 2020, **12**, 6343–6350.
124 P. Zhang, Q. Liao, H. Yao, H. Cheng, Y. Huang, C. Yang, L. Jiang and L. Qu, *J. Mater. Chem. A*, 2018, **6**, 15303–15309.
125 Y. Xu, C. Tang, J. Ma, D. Liu, D. Qi, S. You, F. Cui, Y. Wei and W. Wang, *Environ. Sci. Technol.*, 2020, **54**, 5150–5158.
126 Q. Zhang, H. Yang, X. Xiao, H. Wang, L. Yan, Z. Shi, Y. Chen, W. Xu and X. Wang, *J. Mater. Chem. A*, 2019, **7**, 14620–14628.
127 P. Zhang, Q. Liao, T. Zhang, H. Cheng, Y. Huang, C. Yang, C. Li, L. Jiang and L. Qu, *Nano Energy*, 2018, **46**, 415–422.

128 H. Li, H. Wen, J. Li, J. Huang, D. Wang and B. Z. Tang, *ACS Appl. Mater. Interfaces*, 2020, **12**, 26033–26040.
129 G. Xue, Q. Chen, S. Lin, J. Duan, P. Yang, K. Liu, J. Li and J. Zhou, *Global Challenges*, 2018, **2**, 1800001.
130 M. K. Phadatare and S. K. Verma, *Desalin. Water Treat.*, 2009, **2**, 254–259.
131 P. Zanganeh, A. S. Goharrizi, S. Ayatollahi and M. Feilizadeh, *J. Cleaner Prod.*, 2020, **265**, 121758.
132 K. Zhu and L. Pilon, *J. Quant. Spectrosc. Radiat. Transfer*, 2017, **201**, 53–63.
133 B. Janarthanan, J. Chandrasekaran and S. Kumar, *Desalination*, 2006, **190**, 51–62.
134 B. A. K. Abu-Hijleh and H. A. Mousa, *Energy*, 1997, **22**, 43–48.
135 P. U. Suneesh, R. Jayaprakash, T. Arunkumar and D. Denkenberger, *Desalination*, 2014, **337**, 1–5.
136 L. Zhang, B. Tang, J. Wu, R. Li and P. Wang, *Adv. Mater.*, 2015, **27**, 4889–4894.
137 Z. Wang, T. Horseman, A. P. Straub, N. Y. Yip, D. Li, M. Elimelech and S. Lin, *Sci. Adv.*, 2019, **5**, eaax0763.
138 B. Zhu, H. Kou, Z. Liu, Z. Wang, D. K. Macharia, M. Zhu, B. Wu, X. Liu and Z. Chen, *ACS Appl. Mater. Interfaces*, 2019, **11**, 35005–35014.
139 X. Wang, G. Ou, N. Wang and H. Wu, *ACS Appl. Mater. Interfaces*, 2016, **8**, 9194–9199.
140 C. Xing, D. Huang, S. Chen, Q. Huang, C. Zhou, Z. Peng, J. Li, X. Zhu, Y. Liu, Z. Liu, H. Chen, J. Zhao, J. Li, L. Liu, F. Cheng, D. Fan and H. Zhang, *Adv. Sci.*, 2019, **6**, 1900531.
141 P. Qiao, J. Wu, H. Li, Y. Xu, L. Ren, K. Lin and W. Zhou, *ACS Appl. Mater. Interfaces*, 2019, **11**, 7066–7073.
142 A. K. Menon, I. Haechler, S. Kaur, S. Lubner and R. S. Prasher, *Nat. Sustainability*, 2020, **3**, 144–151.
143 Y. Qin, Y. Wang, X. Sun, Y. Li, H. Xu, Y. Tan, Y. Li, T. Song and B. Sun, *Angew. Chem., Int. Ed.*, 2020, **59**, 10619–10625.
144 G. Li, W.-C. Law and K. C. Chan, *Green Chem.*, 2018, **20**, 3689–3695.
145 X. Wang, Q. Liu, S. Wu, B. Xu and H. Xu, *Adv. Mater.*, 2019, **31**, 1807716.
146 Q. Zhao, C. Du, Y. Jia, J. Yuan, G. Song, X. Zhou, S. Sun, C. Zhou, L. Zhao and S. Yang, *Chem. Eng. J.*, 2020, **387**, 124131.
147 K. Sampathkumar, T. V. Arjunan, P. Pitchandi and P. Senthilkumar, *Renewable Sustainable Energy Rev.*, 2010, **14**, 1503–1526.
148 Z. Deng, J. Zhou, L. Miao, C. Liu, Y. Peng, L. Sun and S. Tanemura, *J. Mater. Chem. A*, 2017, **5**, 7691–7709.
149 M. S. Zielinski, J.-W. Choi, T. La Grange, M. Modestino, S. M. H. Hashemi, Y. Pu, S. Birkhold, J. A. Hubbell and D. Psaltis, *Nano Lett.*, 2016, **16**, 2159–2167.
150 S. Ishii, R. P. Sugavaneshwar and T. Nagao, *J. Phys. Chem. C*, 2016, **120**, 2343–2348.
151 L. Zhou, Y. Tan, J. Wang, W. Xu, Y. Yuan, W. Cai, S. Zhu and J. Zhu, *Nat. Photonics*, 2016, **10**, 393–398.
152 Q. Wang, Z. Zhu, G. Wu, X. Zhang and H. Zheng, *Appl. Energy*, 2018, **224**, 510–526.
153 J. Lou, Y. Liu, Z. Wang, D. Zhao, C. Song, J. Wu, N. Dasgupta, W. Zhang, D. Zhang, P. Tao, W. Shang and T. Deng, *ACS Appl. Mater. Interfaces*, 2016, **8**, 14628–14636.
154 X. Liu, H. Liu, X. Yu, L. Zhou and J. Zhu, *Curr. Opin. Chem. Eng.*, 2019, **25**, 26–34.
155 Y. Li, X. Cui, M. Zhao, Y. Xu, L. Chen, Z. Cao, S. Yang and Y. Wang, *J. Mater. Chem. A*, 2019, **7**, 704–710.
156 M. Gao, C. K. Peh, H. T. Phan, L. Zhu and G. W. Ho, *Adv. Energy Mater.*, 2018, **8**, 1800711.
157 G. Liu, T. Chen, J. Xu, G. Li and K. Wang, *J. Mater. Chem. A*, 2020, **8**, 513–531.
158 P. Yang, K. Liu, Q. Chen, J. Li, J. Duan, G. Xue, Z. Xu, W. Xie and J. Zhou, *Energy Environ. Sci.*, 2017, **10**, 1923–1927.
159 W. Xu, X. Zhou, C. Hao, H. Zheng, Y. Liu, X. Yan, Z. Yang, M. Leung, X. C. Zeng, R. X. Xu and Z. Wang, *Natl. Sci. Rev.*, 2019, **6**, 540–550.
160 P. Xiao, J. He, F. Ni, C. Zhang, Y. Liang, W. Zhou, J. Gu, J. Xia, S.-W. Kuo and T. Chen, *Nano Energy*, 2020, **68**, 104385.
161 X. Li, X. Min, J. Li, N. Xu, P. Zhu, B. Zhu, S. Zhu and J. Zhu, *Joule*, 2018, **2**, 2477–2484.
162 L. Zhu, T. Ding, M. Gao, C. K. N. Peh and G. W. Ho, *Adv. Energy Mater.*, 2019, **9**, 1900250.
163 G. Xue, Y. Xu, T. Ding, J. Li, J. Yin, W. Fei, Y. Cao, J. Yu, L. Yuan, L. Gong, J. Chen, S. Deng, J. Zhou and W. Guo, *Nat. Nanotechnol.*, 2017, **12**, 317–321.
164 Q. Guan, Z. Han, Z. Ling, H. Yang and S. Yu, *Nano Lett.*, 2020, **20**, 5699–5704.

